This is the Pre-Published Version.
This is the accepted version of the work. The final published article is available at https://doi.org/10.1139/cgj-2019-0322.

A coupled CFD-DEM investigation of internal erosion considering suspension flow

Author 1

Yajing LIU, PhD candidate

Key Laboratory of Offshore Geotechnics and Material of Zhejiang Province, College of Civil Engineering and Architecture, Zhejiang University, China

Email: yajing_liu@zju.edu.cn

Author 2

Zhen-Yu YIN*, Associate Professor

Department of Civil and Environmental Engineering, The Hong Kong Polytechnic University, Hung Hom, Kowloon, Hong Kong, China

Email: zhenyu.yin@polyu.edu.hk; zhenyu.yin@gmail.com

Author 3

Lizhong WANG, Professor

Key Laboratory of Offshore Geotechnics and Material of Zhejiang Province, College of Civil Engineering and Architecture, Zhejiang University, China

Email: wanglz@zju.edu.cn

Author 4

Yi HONG, Associate Professor

Key Laboratory of Offshore Geotechnics and Material of Zhejiang Province, College of Civil Engineering and Architecture, Zhejiang University, China

Email: yi_hong@zju.edu.cn

***Corresponding author:**

Zhen-Yu YIN, Tel: +852 3400 8470; Fax: +852 2334 6389; Email: zhenyu.yin@polyu.edu.hk; zhenyu.yin@gmail.com

Abstract: The influence of two-phase flows containing suspension particles, which are common in nature, on internal erosion with coupling effect of clogging remains unclear. This paper presents a three-dimensional coupled discrete element method and computational fluid dynamics (CFD-DEM) analysis of internal erosion considering different concentrations of suspension *C* (i.e., mass of the suspended particles in unit volume of fluid) in gap-graded granular soils with different fine fraction F_c (i.e., the percentage by mass of the fine particles in the gap-graded sample). The influences of *C* and F_c on the erosion and clogging behavior of soils are investigated from both the macroscopic and microscopic perspectives. It is found that for gap-graded samples being under-filled with F_c=15%, the suspension flow (i.e., influent fluid with suspending particles) decreases the cumulative eroded fine particle loss and the increasing rate of soil hydraulic conductivity due to clogging at the top of the sample. The degree of clogging is found to jointly be determined by both constriction size distribution and the suspension concentration. Clogging in a local area usually occurs with the formation of the clusters which has a high resistance to the drag force applied by the fluid flow.

Keywords: gap-graded soil, erosion, clogging, suspension, fine fraction, constriction size

1. Introduction

Internal erosion may occur when the coarse grain group of a gap-graded sandy soil is unable to prevent the erosion of the fine particles under the action of seepage. This issue has been studied extensively by various researchers (Skempton and Brogan, 1994; Indraratna et al., 2007; Chang and Zhang, 2013; Shire et al., 2014; Santos et al., 2015; Benamar et al., 2019; Yang et al., 2019, 2020). The geometrical condition, hydraulic loading and in-situ stress conditions, i.e., the gap ratio (i.e., the ratio of the minimum particle diameter in the coarse grain group to the maximum particle diameter in the fine grain group), fine fraction (F_c), hydraulic gradient (i) and mean effective stress (p') are identified as the most influential factors that govern the initiation and evolution of internal erosion.

Previous studies on internal erosion usually assumed that the inflow applied to the sample is pure fluid without any suspension particles. In reality, the seepage flow through soils usually contains dispersed suspension particles with the size ranging from fractions of a millimeter down to macromolecular dimensions (Amir and Brij, 2009). The presence of the suspension particles within the inflow is may eventually cause to cause clogging in the gap-graded soil, with consequences to change the soil structure, the hydraulic properties and mechanical behavior of the soil. The seepage flow containing suspension particles could either destabilize the primary load-bearing structure to weaken the soil strength by inducing dislodgement of soil grains (Hicher, 2013; Yin et al., 2014, 2016;), or strengthen the primary fabric to increase the soil strength by introducing more load-bearing fine particles into the gap-graded soil. As far as the hydraulic property is concerned, the seepage flow containing suspension particles is likely to reduce the void ratio and soil hydraulic conductivity (Alem et al., 2015; Sato and Kuwano, 2015; Yang et al., 2020), by single-particle plugging or by particulate bridging at pore throats (Valdes and Liang, 2006). Limited experimental data have shown that the soil hydraulic conductivity could be reduced by more than 50% by seepage flow containing a low concentration (e.g., 0.5 g/L) of suspension particles (Reddi et al., 2005). Thus, the seepage flow containing suspension particles could have significantly affected the hydro-mechanical behavior of granular soils during internal erosion.

Although many significant macroscopic phenomena have been obtained from the existing experimental investigations, a limited number of numerical studies have been performed to understand the underlying microscopic mechanisms for the experimental observations. As a result, some important microscopic insights of internal erosion and clogging, e.g., the transportation or distribution of suspension particles within gap-graded samples has yet not been well understood. Due to the complex interactions between the fluid and soil particles during the coupled processes of erosion and clogging, the numerical methods which only capture single-phase behavior (either for the solid or liquid phase) are insufficient for the purpose. A combination of computational fluid dynamics (CFD) and the discrete element method (DEM) has been emerging as a powerful tool for modeling the particle-fluid system in recent studies (Zhao and Shan, 2013; Zhao et al., 2016; Kawano et al., 2018; Hu et al., 2019).

This paper aims to study the influence of seepage flows containing suspension particles on the clogging, erodibility and hydro-mechanical behavior of granular soils from both macro- and microscopic perspectives, through a 3D coupled CFD-DEM investigation. Key influence factors considered in the numerical analyses include suspension concentrations in the seepage flow (C), fine fraction in the gap-graded soil (F_c) and hydraulic gradient (i). Macroscopic observations in various aspects, including cumulative eroded particle mass, sample deformation, hydraulic conductivity, erosion rate and stress-strain relations, are presented with their responses to different C and F_c. The microscopic mechanisms underpinning these macroscopic observations are also analyzed, in the context of transportation and clogging of suspension particles within gap-graded samples, the evolution of load-bearing structure and constriction size distributions.

2. Coupled CFD-DEM method

The coupled CFD-DEM method used in this study includes formulations for three key elements, i.e., the discrete element method (DEM), computational fluid dynamics (CFD) and the coupling between CFD and DEM. In this study, the open-source DEM code LIGGGHTS 3.7.0 (Kloss et al., 2012) and CFD code OpenFOAM 5.0 (Jasak et al., 2007) are adopted for simulating massive dispersed particle bodies and hydrodynamic processes, respectively. The particle-fluid interaction forces, including the drag force, pressure gradient force and viscous force, are computed by coupling the CFD and DEM codes (Goniva et al., 2012; Kloss et al., 2012). Governing equations for DEM, CFD, and coupling between CFD and DEM have been given elsewhere (Hu et al., 2019), and are summarized in the Appendix.

The coupled CFD-DEM method is validated according to Chang (2012), in which a series of internal erosion tests were performed on real gap-graded granular soil under different effective confining stresses (σ'_c) and hydraulic gradients (i). Considering the similarity between Chang (2012) and this study in the stress and hydraulic conditions, the experimental results reported in Chang (2012) are used here to validate the numerical

CFD-DEM model. In some cases of the experiment, the specimen was tested under isotropic stress states with mean effective stress (p') of 50 and 200 kPa. The hydraulic gradient, i, was increased in stages from 0 to the final value (i.e., 0.15 per 10 minutes for i<1.0, 0.25 per 10 minutes for 1.0<i<2.0, and 0.50 per 10 minutes for i>2.0). More details are introduced in Chang (2012).

Fig. 1 shows the grain size distribution of the gap-graded granular materials with F_c=35% used in the experiment and validation model. The gap-graded material with F_c=15% and 35% in Fig. 1 is adopted in the analysis of internal erosion with suspension particles. The material with a low gap ratio and a narrow range of grain diameter is used in the simulation to reduce the total number of DEM particles and improve calculation efficiency. For the sake of computational efficiency, the hydraulic gradient in simulations was increased by one level every 2.0 s. Although the simulation duration is very short compared with that in the laboratory test, the simulated results below show that it is sufficient to reproduce the experimental results in trend. Table 2 summarizes the parameters used in the validation model.

Fig. 2(a) shows the simulated and experimental results for the cumulative eroded particles mass during erosion. Both simulated and experimental results present that the specimen under p'=200 kPa has a higher critical hydraulic gradient and a larger final cumulative eroded particles mass compared with those of the specimen under p'=50 kPa. The tests showing intensified erodibility of the samples by higher p', e.g., the cumulative eroded particles mass increasing with p', are also reported by Bendahmane et al. (2008). Figs. 2(b) and 2(c) show the vertical strain and transverse strain of the samples under p'=50 and 200 kPa. The simulated results are in good agreement with the experimental results in trend, which demonstrates the predictive capability of the CFD-DEM method for capturing the main characteristics of soil behavior during internal erosion. The scatters between the measured and simulated results are probably caused by some simplifications of the numerical model, e.g., the difference in gradation between the experimental and numerical soils, spherical particles, short simulation time, etc.

The critical *i* for the occurrence of internal erosion in the simulations is smaller than that of the experiments. This is because all particles in the simulations are spherical, for which the voids formed by coarse particles are larger than that formed by the real soil particles with non-spherical shape, e.g., flat, ellipse or prism. The spherical fine particles are also more likely to get through the voids formed by the coarse particles and hence eroded under the action of seepage flow. The influences of particle shape on erosion will be analyzed in future work.

3. Simulation program and model setup

3.1 **Simulation program**

The simulation program includes 12 cases to study the effects of suspension concentration (i.e. particle concentration in pore fluid according to Reddi et al. (2005) where particles are not contacted each other), fine fraction in the gap-graded soil and hydraulic gradient on internal erosion, as summarized in Table 1. Fig. 1 shows the particle size distributions of the two gap-graded samples with F_c=15% and 35% for the current study. It is inferred from the previous studies (Skempton and Brogan, 1994; Minh et al., 2014; Shire et al., 2014) that, for samples with F_c=15%, the fine particles are likely to under-fill the voids between coarse particles and play a diminished role in stress transfer. In contrast, when the fine fraction exceeds about 25% (e.g., 35%), the fine particles are found to start overfilling the voids between coarse particles, to carry loads for stabilizing the force transmission structures. Thus, the gradations used in this study represent two typical fabrics of the gap-graded sandy soil. According to Burenkova method (1993), the soil is internal unstable (i.e., internal erosion occurs when the hydraulic gradient reaches the critical hydraulic gradient) if d_{90}/d_{60} of the soil satisfies the following equations:

$$0.76\log\left(d_{90}/d_{15}\right)+1<d_{90}/d_{60}<1.86\log\left(d_{90}/d_{15}\right)+1 \quad (1)$$

where d_{15}, d_{60} and d_{90} are the sizes of grain at which 15%, 60% and 90% of particles by weight are smaller, respectively. Fig. 3 shows the assessment of internal stability for the samples with F_c=15% and 35% by Burenkova method. It is shown that both samples are susceptible to internal erosion. In this study, the suspension particles are assumed to come from the upstream soil (Goldsztein, 2005). The suspension particle size distribution in the influent is the same as that of the fine fraction of the sample. This study focuses on the influence of the physical clogging of suspension particles on the internal erosion of the gap-graded soil. The cohesion of the suspension particles is not considered. Some previous studies (Zamani, 2009; Zheng et al., 2014) on pore-clogging by the suspension particles also did not take into account the cohesion of suspension as an influential factor.

The previous experiments (Skempton and Brogan, 1994; Li, 2008) have shown that the i_c is usually smaller than 0.3 for coarse-grained soils. Thus, the hydraulic gradient i=0.10, 0.25 was selected in this study, which broadly covers the typical ranges of the critical hydraulic gradient for the initiation of internal erosion. Two relatively high suspension concentrations, i.e., of 30 and 60 g/L, are selected in this study to facilitate clogging of suspension particles in a short simulation time (15.0 s). During the entire simulation process, a constant isotropic pressure (p') of 50 kPa is posed to each sample. Internal erosion where fine particles are washed out the soil matrix can happen in different directions of flow. The current study focuses on the downward migration of the fine particles, which usually occurs on the supported side of the retaining wall. As the maximum pressure induced by the gravity force (lower than 1 kPa) is significantly lower than the 50 kPa of confinement (Kawano et al., 2018), the gravity force is not considered in this study to eliminate its influences on the particle detachment and migration (Wautier et al., 2019; Hu et al., 2019). In this case, a lot of fine particles within the sample are floated or only have one contact, which further decreases the critical i of the sample.

3.2 **Model geometry and parameters**

Fig. 4 shows a cuboid sample consisting of spherical particles, with a size of 13 mm×13 mm×26 mm ($14D_{50}\times14D_{50}\times28D_{50}$). D_{50} is the diameter at 50% mass passing. The CFD domain overlaps the DEM domain with a size of 13.5 mm×13.5 mm×35 mm. An upstream region with a size of 13 mm×13mm×5 mm was defined on the top of the cuboid sample to generate dispersed suspension particles (SPs) in the influent. The CFD domain is larger than the DEM one to ensure that all particles in the sample are immersed in the fluid and subjected to the fluid-particle interaction forces. In the coupled CFD-DEM method, the boundary conditions applied on CFD and DEM domains are in fact independent with each other. Each domain has its independent boundary conditions to ensure a correct calculation for granular materials or fluid flow. To maintain a constant particle concentration, the number of the suspension particles in the upstream region was regulated for each 0.01 s during the entire simulation period (15.0 s). The parameters for the particle properties, i.e., elastic modulus (E), friction coefficient (u_f) and rolling friction coefficient (u_r), are adopted according to previous DEM studies modeling the mechanical behavior of sand (Wang and Gutierrez, 2010; Yang et al., 2017). The rolling friction impedes the rotation of particles, which certainly prevents the detachment and migration of the fine particles to some degree. In this study, the value of rolling friction is 0.1 which is typically adopted in some previous numerical studies on granular materials (Goniva et al., 2012; Yang et al., 2017). Some cases without rolling friction are also simulated to reveal its influences on internal erosion preliminarily, which is shown in section 4.1. The time step in CFD and DEM is adopted as 1×10^{-4} s and 5×10^{-7} s, respectively. The difference in the size of time step in CFD and DEM is larger compared to other CFD-DEM coupling studies on internal erosion (e.g. Hu et al. 2019, Nguyen and Indraratna 2020(a)). Nevertheless, Zhao and Shan (2013) found that the numerical results of the coupled CFD-DEM method agree well with the analytical solutions of one-dimensional consolidation when the time step in CFD and DEM equals 5×10^{-4} s and 5×10^{-7} s, respectively. Table 2 summarizes the simulation settings.

3.3 **Boundary conditions**

In each numerical analysis, constant differential pressure between the inlet and outlet boundaries of CFD domain was applied to maintain the hydraulic gradients ($i=\Delta p/\rho gL$, where Δp is the differential pressure and L is the sample length in the flow direction) of i = 0.10 or 0.25 across the sample length. Free slip boundary conditions were applied on the four lateral walls, meaning that the surface fluid was restricted to move along the wall.

For the boundary conditions of DEM, an isotropic stress of p'=50 kPa was applied to each DEM sample using a servo wall algorithm. The friction coefficient of the confining wall was 0 while its elastic stiffness was 10 times larger than that of the particle. The friction of the wall is set as 0 to prevent the generation of shear stress at the boundary of the sample, which is also adopted in some previous numerical research on interna erosion with the coupled CFD-DEM method (Wautier et al., 2018; Wautier et al., 2019). If the wall is relatively smooth, previous studies show that it is likely to facilitate the erosion of the fine particles near the wall and decrease the critical hydraulic gradient (Moffat et al., 2011; Nguyen and Indraratna, 2020(a)). A perforated base plate with a 0.5 mm pore-opening size (1.5 times of the diameter of the largest fine particle) is placed underneath each sample to allow the migration of the fine particles only.

3.4 **Simulation procedure**

A cuboid assembly of spheres was first generated randomly with the prescribed gradation (Fig. 1) and compacted by six surrounding walls under the 50 kPa confinement. The inter-particle friction coefficient was maintained at a relatively low value of 0.1 during the sample preparation processes (i.e., generating particles and applying isotropic pressure to the sample) to generate a relatively dense sample. After the sample preparation and before applying seepage flow, the inter-particle friction coefficient is increased to 0.3.

After the generation of the initial DEM sample, a differential hydraulic pressure was imposed on the upstream and downstream of the sample to model internal erosion. Simultaneously, the dispersed suspension particles were generated periodically in the upstream region. The information of each particle (including position, velocity and drag force) and contact (including the positions of particles in contact and contact force) were recorded every 0.05 s during the entire simulation. Each simulation that models 15 seconds of physical time of erosion in this study took approximately 5~7 days on an HP workstation with 8 Intel Xeon E52680-v4 2.4GHz processors and 512GB DDR4 RAM. The simulation duration (i.e., 15 s) is relatively short as compared to that in a laboratory test. Nevertheless, the numerical results presented below show that this duration has largely covered the key stages for internal erosion involved in each analysis, i.e., initiation and a gradually stabilized response. The key macro- and microscopic mechanisms on the internal erosion of gap-graded soil are contained in each simulation reported herein.

4. Numerical results and discussion

4.1 **Net cumulative fine particle loss**

Fig. 5(a) shows the percentage of the net cumulative fine particle loss (m_{e_net}=m_e-m_{in}, where m_e and m_{in} denote the percentage by mass of the particles flowing out and into the sample, respectively) for the samples with F_c=15% under different C and i. It is found that a higher hydraulic gradient facilitates the internal erosion for the sample under the same concentration because of larger drag forces applied to fine particles. The existence of the suspension particles decreases the net fine particle loss compared with that in the case of C=0. This is because the fine particles under-fill the voids between coarse particles for the sample with F_c=15%, leading to an easier occupation of the remaining space by the suspension particles. Higher suspension concentration increases the influx of the suspension particles (the mass of suspension particles through the unit cross-sectional area within a unit time), facilitating clogging at the top of the sample and impeding the development of internal erosion. Figs. 5(b) and 5(c) show that the development of the vertical and transverse strains of the sample with F_c=15% during erosion. The transverse strain in this study is defined as the average value of the strain in two horizontal directions (i.e., the ratio of the change in the width of the sample to its original width). The sample deformations in different cases are slightly affected by the erosion of the fine particles because the sample of F_c=15% is mainly composed of contacts between coarse particles.

Fig. 6 compares the cumulative eroded fine particle loss in the case of i=0.25 and F_c=15% under different concentrations and rolling friction. Although the incorporation of the rolling friction decreases the eroded fine particle loss for each case, the trend for the eroded fine particle loss under different concentrations is unchanged. In other words, it is reasonable to assume that the effects of rolling friction and suspension concentration are independent.

Fig. 7(a) shows the percentage of the net cumulative fine particle loss (m_{e_net}) for the sample with F_c=35%. Comparing Fig. 5(a) to Fig. 7(a), the m_{e_net} of the sample with F_c=35% also increases with the hydraulic gradient but varies slightly under different suspension concentrations. For the sample with a high fine fraction (e.g., F_c=35%), the fine particles overfill the voids between coarse particles, preventing the entry of the suspension particles to the sample. Figs. 7(b) and 7(c) show the development of vertical and transverse strains of the sample with F_c=35% during erosion. Although the m_{e_net} of the samples with F_c=15% (m_{e_net}=0.6%~3.5%) is two or three times larger than that of the samples with F_c=35% (m_{e_net}=0.75%~1.8%), the strain level of the former (i.e., 0.005%~0.16%) is much smaller than that of the latter (i.e., 0.2%~1.6%) because of the different types of their material fabrics. For the sample with F_c=15%, the coarse particles are in contact with each other while most fine particles are confined within voids between coarse particles, providing little support to the coarse particles (Skempton and Brogan, 1994; Minh et al., 2014; Shire et al., 2014). Thus, the erosion of the fine particles has rarely affected the stability of the coarse particle supported fabric which mainly carries the external pressure (p'=50 kPa in this study). For the sample with F_c=35%, however, the coarse particles are dispersed within a matrix of fine particles (Skempton and Brogan, 1994; Minh et al., 2014; Shire et al., 2014). Then the erosion of the fine particles leads to the rearrangement of the coarse particles and hence a relatively large deformation of the entire sample.

Fig. 8 shows the erosion rate in terms of mass percentage for the samples with F_c=15% and 35% under different suspension concentrations (C) and hydraulic gradients (i). For the samples with F_c=15%, the fine particles are susceptible to be eroded under a higher i and a lower C. The suspension concentrations (C) have a slight influence on the erosion rate for the sample with F_c=35%, as similar to the behavior of cumulative eroded fine particle loss (Fig. 7(a)). The erosion rate for both samples under each condition is relatively larger at the beginning of internal erosion and then gradually decreases until the end of the simulations. This behavior is also observed in previous experiments (Chang, 2012), which demonstrates the predictive capability of the CFD-DEM method for capturing the main characteristics of internal erosion in a limited simulation time (i.e., 15 s).

4.2 **Vertical distribution of fine fraction**

Fig. 9 shows the distribution of fine fraction along the height of the samples with F_c=15% and 35% after the action of seepage with different C and i. For the sample F_c=15% and C=0, Fig. 9(a) shows that the fine fraction near the top of the sample is smallest compared with that near the middle and bottom, suggesting that the fine particles near the top are dragged downward by the seepage force. This phenomenon is consistent with the experimental observations reported by Chang and Zhang (2013) and Nguyen et al. (2019). When the influent contains the suspension particles (C>0 g/L), the fine fraction along the full height of the sample increases due to the deposition of the suspension particles. However, the suspension particles are mostly retained near the top of the samples.

Fig. 9(b) shows that the fine particles at the top of the sample with F_c=35% are eroded the least in all cases. This is because the fine particles in this sample overfill the voids between coarse particles, leading to a higher number of fine contacts with stronger contact forces than the fine particles in the sample with F_c=15% (Shire et al., 2014), making the fine particles in the former less vulnerable to detachment and migration. Comparing to the fine particles near the top of the sample with F_c=35%, the fine particles near its bottom (i.e., the outlet) are prone to be eroded as shown in Fig. 7(b). This also agrees with previous experimental findings (Valdes and Santamarina, 2007; Bendahmane et al., 2008). A weak erosion of the fine particles at the top of this sample prevents the entry of the suspension particles, results in a slight increase of the fine fraction at the top region in the case with large concentrations (C=30 and 60 g/L).

4.3 **Results on hydraulic conductivity**

Figs. 10(a) and 10(b) show the evolution of the overall hydraulic conductivity for the whole samples with F_c=15% and 35% under different C and i, respectively. The hydraulic conductivity (k) considered in this study is defined as follows:

$$k = \frac{q}{Ai} \tag{2}$$

where q is the flow rate. i is the hydraulic gradient along with the sample height. A is the cross-section of the sample. Each value of instantaneous hydraulic conductivity k during erosion is normalized by the initial value k_0 of the corresponding sample before erosion. For the sample with F_c=15%, its hydraulic conductivity increases with i. This is because higher i induces more fine particle loss (see Fig. 5(a)) and hence a larger increase of the void ratio or porosity. The porosity-dependent hydraulic conductivity has been well recognized and formulated in the literature, e.g., Scheidegger (1960)'s formulation that correlates porosity (ϕ) to soil hydraulic conductivity k, as follows:

$$k = \frac{C_s}{\tau^2 S_s^2} \frac{\phi^3}{(1-\phi)^2} \tag{3}$$

where C_s is the empirical shape factor, S_s is the specific surface area per grain volume, which is defined as the ratio between the total surface area ΣS_i and the total volume ΣV_i of particles in each sample. τ is the tortuosity (=L_a/L; where L_a is the average length of the fluid path, L is the geometrical length of the sample that fluid flows through), and ϕ is the soil porosity. The S_s and ϕ are calculated by the radius of the current particles in each sample which are directly output by the DEM code. The tortuosity in Eq. 3 is one of the most abused parameters due to the lack of understanding and the lack of proper ways to measure it. Therefore, hydraulic tortuosity is often treated merely as a fitting factor, or worse (Han et al., 2018). In this study, the tortuosity (τ) is estimated as follows:

$$\tau = \frac{\Delta L_a}{\Delta L} = \frac{\Delta L_a / \Delta t}{\Delta L / \Delta t} = \frac{\overline{v}_a}{v_D} \tag{4}$$

where ΔL_a and ΔL are the average path and the geometrical length of the sample that fluid flows through per unit time Δt, respectively. $\overline{v}_a$ and v_D are the average pore flow velocity and Darcy flow velocity, respectively. $\overline{v}_a$ is estimated by the average flow velocity of all the CFD cells. v_D equals q/A, where q is the flow rate obtained directly from the CFD code and A is the cross-section area of the sample. To evaluate the above approach for τ, the evolution of the values of τ calculated by Eq. 4 (this study) is compared with the results calculated by the method proposed by Nguyen and Indraratna (2020(b)) for each case. Eq. 5 is the equation proposed by Nguyen and Indraratna (2020(b)) to estimate the tortuosity of granular materials, which is derived from back-analysis based on experimental data.

$$\tau = p(1 - \ln(n)) \tag{5}$$

where n is the porosity of the sample, p=0.6 and 1.15 for spheres and natural sand. Considering that all particles in this study are spherical, p=0.6 is therefore adopted.

For the samples with F_c=15%, Fig. 11(a) shows that the τ calculated by both the approach in this study and that of Nguyen and Indraratna (2020(b)) in each case decreases during internal erosion due to the fine particle loss and the accompanying increase of the sample porosity (n). Besides, the decrease of τ estimated by the approach in this study is larger than that of Nguyen and Indraratna (2020(b)). It is probably because Eq. 5 is derived from non-gap-graded soils and thus unable to consider the contribution of the local erosion zone (see Fig. 12(a) and 12(b)) to the decrease of τ. The scatters between the two methods exist because both of them are indirect estimations of τ. Similarly, Fig. 11(b) shows that the τ for the samples with F_c=35% in each case still decreases at the end of the internal erosion. The slight increase of τ at the initial stage in the case of i=0.10 is primarily due to the clogging of the suspension particles at the top of the samples.

Fig 10 shows the calculated hydraulic conductivity for each sample according to Kozeny-Carman equation, i.e., Eq. 3. It can be seen that the equation has broadly captured the evolution of hydraulic conductivity with the change of porosity resulting from the internal erosion in different samples. Note that scatters between the calculated and the computed results could be found due to the heterogeneity of the fine fraction and void ratio within the sample subjected to internal erosion (Sterpi, 2003; Sibille et al., 2015). On the other hand, the clogging area (analyzed in the section below) within the sample possibly has a strong effect on the prevention of the fluid flow and hence decreases the hydraulic conductivity further, which can't be reflected in the theoretical equation.

4.4 **Migration of fine particles and evolution of constriction size distribution**

Fig. 12 shows the configuration of the sample packing and streamlines for the samples with F_c=15% and F_c=35% under i=0.25 and C=30 g/L at the beginning and the end of the simulation. For the sample with F_c=15%, Figs. 12(a) and 12(b) show that the specific zones where fine particles have been washed out completely (only the coarse particles remained) develop from the top and then progress the downwards. This is consistent with the experimental findings of Chang (2012) and Ke and Takahashi (2014). It is worth noting that the flow in the erosion zone, as shown in the black square frame in Fig. 12(b), has a larger flow velocity due to larger void space compared with that of the surrounding zone. The erosion amount in the region is also larger, suggesting that the fine particles are eroded through an erosion channel rather than uniformly pass through a transection of the sample. This is usually caused by a partial clogging of the interstitial space outside the erosion channel (Sterpi, 2003; Sibille et al., 2015). The streamlines in Fig. 12 (b) show that the fluid flow within the sample with F_c=15% has a significant heterogeneity in terms of flow velocity and direction at the end of the simulation, which is caused by the inhomogeneous distribution of the fine particles within the sample. Fig. 12 (b) also shows the average fluid velocity of the fluid cells along with the sample height. At the height with erosion region, as shown in the black frame, the average fluid velocity is correspondingly larger, which is consistent with the results presented by the streamlines in Fig. 12 (b).

Figs. 12(c) and 12(d) show that for the sample with F_c=35%, the inhomogeneous migration of the fine particles is less apparent at the end of the simulation compared with that of the sample with F_c=15%. The reason for this phenomenon includes two aspects. First, the detachment of the fine particles is restricted due to stronger contact forces and a higher number of contacts between the fine particles. On the other hand, the overfilled voids between the coarse particles leave small space for free migration of the fine particles, preventing their gradual accumulation in a local zone and hence the occurrence of clogging. Due to a relatively uniform fine particle distribution, the fluid flow within the sample is also relatively uniform in terms of flow velocity and direction at the beginning and the end of the erosion process.

Previous researches (Indraratna et al., 2007; Indraratna et al., 2015) reveal that the constriction size (diameter of the constriction constituted by the coarse particles) formed by the coarse particles controls the detachment, migration and clogging of fine particles. A criterion based on the constriction size distribution constituted by the coarse particles is also proposed to evaluate the internal erosion for granular filters (Indraratna et al., 2007). In this study, the constriction size is calculated by the method proposed by Shire and O'Sullivan

(2016). This method first partitions the sample using a three dimensional weighted Delaunay tessellation with the tetrahedra vertices being located at the particle centroids. On each tessellation face the constriction size is then assumed to be the diameter of the circle that can be inscribed between particles. If two inscribed circles overlap to some extent, they are merged and deemed as a constriction (Shire and O'Sullivan, 2016).

Fig. 13 shows the evolution of the distribution of the constriction size formed by the coarse and fine particles in the erosion and clogging areas in the case of F_c=15%, i=0.25 and C=60 g/L. The insets of Figs. 12(a) and 12(b) show the evolution of the local packing configuration for the erosion and clogging areas, respectively. In the erosion area (Fig. 13(a)), the fine particles are gradually lost while coarse particles remain stationary in the erosion process. In contrary to the erosion area, the fine particles gradually accumulate within the voids between three or four coarse particles in the clogging area (Fig. 13(b)). The probability of the small constriction size increases gradually in the clogging area but decreases in the erosion area during erosion, which is consistent with the evolution of the local packing configurations for these two areas, as shown in the insets of Fig. 13.

4.5 **Micromechanical analysis on clogging**

The micromechanical analysis on the clogging phenomenon caused by suspension particles enables a better understanding of the macro observations, i.e., the cumulative fine particle loss and the deformation of the samples under different C (Figs. 5 and 7). It is also beneficial to reveal new insights into internal erosion with the suspension concentration. Fig. 13(b) shows that in the clogging area, the fine particles are gradually accumulated and formed as a cluster. The fine particles in a cluster have a larger coordination number, which contributes to preventing the detachment and migration of these particles. The coordination number is defined in Eq. 6, as follows:

$$Z = \sum_{i=1}^{N_p} \left(\frac{C_i}{N_p} \right) \quad (6)$$

where C_i is the number of contacts between particle i and other particles; N_p is the total number of particles. On the other hand, the size of the cluster is also larger than the diameter of the voids between coarse particles, which contributes to the resistance of both the entire cluster and single fine particle to internal erosion. To quantify the micro-parameters of the cluster, Fig. 14 compares the coordination number and the number density of the fine particles (i.e., the number of the fine particles per unit volume within the sample) in the cluster (Fig. 12(b)) and the entire sample. During internal erosion, the coordination number and the number density of the fine particles in the cluster are both larger compared with the mean value of the sample. These microscopic properties of the cluster validate previous analyses on its clogging mechanism.

Considering that most of the suspension particles are retained near the top of the sample, the top region with a height of 10 mm (about the two-fifths height of the sample) is divided into eight sub-regions, as shown in the inset of Fig. 14. The retention ratio of the fine particles (R_{ret}) is used here to characterize the degree of clogging in each sub-zone, which is defined as follows:

$$R_{ret} = \frac{N_{pc}}{N_{pt}} \quad (7)$$

where N_{pc} is the number of the suspension particles retained in a region after erosion. N_{pt} is the total number of the suspension particles that flow through a region in the entire process of erosion. The coefficient of variation (i.e., the ratio of the standard deviation to the mean) for the constriction sizes of the eight sub-regions is about 0.01, suggesting that the packing in these selected regions is relatively uniform. However, the retention ratios R_{ret} of the eight sub-regions are quite different (varying from 0.48 to 0.79), implying that the mean constriction size alone is insufficient to determine whether the suspension particle would be retained or eroded.

Fig. 15 shows the initial constriction size distribution constituted by the coarse particles and the retention ratio in each sub-region. A statistical parameter, i.e., the cumulative probability of the mean constrictions (P_{mean}), is proposed in this study to analyze the influence of the constriction size distribution on the retention ratio. Generally, Fig. 15 shows that the fine particles are prone to be retained in the sub-region with a larger P_{mean}. This is because the fine particles have a larger probability to flow through a small constriction in a region with a larger P_{mean} and hence to plug or bridge at the small constriction. A gradual decrease of the constriction size caused by the clogging of the fine particles in turn leads to more retention of the fine particles flowing through the sub-region. It is also revealed from the figure that a slight heterogeneity of the initial constriction size distributions in different regions can lead to quite different mechanical responses during the internal erosion.

Nevertheless, the R_{ret} in each sub-region is not only determined by its initial constriction size distribution. For instance, the region B2 has the smallest P_{mean}=66% but its R_{ret} is much larger than region B1 and B4 with P_{mean}=68%. Fig. 17 shows a schematic contour of R_{ret} for the eight sub-regions, considering the P_{mean} and the suspension concentration. Although the suspension particles are distributed uniformly in the influent, as shown in Fig. 4, the number of suspension particles in each sub-region varies due to the heterogeneous fluid flow and tortuosity (Moffat et al., 2011; Bacchin et al., 2014). Therefore, the suspension concentration in each sub-region is defined as the time-average concentration in the entire erosion process. It can be observed that the sub-regions with a smaller P_{mean} may experience a higher R_{ret}, because of a higher concentration of the suspension flow in these sub-regions.

Fig. 17(a) shows the distribution of the suspension particles, the particle-fluid interaction forces applied to them, and the streamlines in the case of F_c=15%, C=70 g/L, and i=0.25 at the end of erosion. The suspension particles at the bottom of the sample (i.e., the particles with a larger migrated distance) are subjected to comparatively larger particle-fluid interaction forces. Conversely, for the suspension particles clogged at the top of the sample, the particle-fluid interaction forces applied to them are smaller. These results suggest that the suspension particles subjected to larger particle-fluid interaction forces are more likely to migrate longer distances while the particles subjected to smaller particle-fluid interaction forces probably accumulate together (i.e., form cluster) and lead to the occurrence of clogging. The particle-fluid interaction force on a particle is determined by the flow velocity of the fluid around it, as shown in the streamlines in Fig. 17(a). The particles with larger particle-fluid interaction forces are usually located in a region with larger flow velocity. The heterogeneous evolution of the flow velocity within the sample may be affected by a slight difference in the initial constriction size distribution and fine particle distribution among different sub-regions, which is an interesting topic and will be analyzed in the future work.

To quantitatively address the influences of the hydraulic drag forces acting on particles on soil migration, Fig. 17(b) shows the relationship between the particle-fluid interaction force averaged over time and migration distance for the suspension particles. Most suspension particles subjected to larger particle-fluid interaction force migrate longer within the sample, which is consistent with the results as shown in Fig. 17(b).

5. Conclusions

This paper presents the micro-macro investigation from a 3D coupled CFD-DEM analysis of internal erosion in gap-graded granular soils, with particular consideration of suspension flow. Two typical gradations, i.e., samples under-filled and overfilled with fine particles (fine fraction F_c=15 and 35%, respectively), were considered under the conditions of different hydraulic gradients and suspension concentrations. Micro-scale variables were studied to investigate the influence of the suspension concentration on the internal erosion behavior of soils and the occurrence of clogging. Based on the analyses of all simulation results, the following conclusions can be made:

(1) For the sample under-filled with fine particles (F_c=15%), the suspension flow decreases the cumulative eroded fine particle loss and the increasing rate of soil hydraulic conductivity due to clogging near the top of the sample. For the sample with F_c=35%, the fine particles overfill the voids between coarse particles, preventing the entry of the suspension particles to the sample. In this case, the suspension flow has slight influences on the erosion behavior of the sample.

(2) Due to the heterogeneous nature of internal erosion, a slight heterogeneity of the initial constriction size distributions in different regions can lead to quite different mechanical responses during the internal erosion for different sub-regions, i.e., the formation of the erosion area and clogging area. The probability of the small constriction size increases

gradually in the clogging area but decreases in the erosion area during erosion.

(3) The clogging degree, characterized by the retention ratio, is found to depend on both the constriction size distribution and the suspension concentration. A big cumulative probability of the mean constriction size (P_{mean}) facilitates the capture of suspension particles. A high suspension concentration in internal erosion increases the probability of the contacts between suspension particles, which also contributes to the capture of the particles and facilitates the occurrence of clogging.

(4) The particles in a cluster have a high resistance to the drag force exerted by the fluid flow. Firstly, the fine particles in a cluster have a larger coordination number than that of the fine particles outside the cluster, which helps to stabilize the fine particles in the cluster. Secondly, the size of a cluster is much larger than the diameter of the voids between the coarse particles, preventing further migration of the fine particles.

Acknowledgement

The work presented in this paper is supported by the GRF project (Grant No. 15209119) from Research Grants Council (RGC) of Hong Kong. National Key Research and Development Program of China (2016YFC0800200) and National Natural Science Foundation of China (51939010 and 51779221).

Appendix: Coupled CFD-DEM method

Governing equations for DEM

At any time *t*, the equation governing the translational and rotational motion of particle *i* is

$$\begin{cases} m_i \dfrac{d\mathbf{U}_i}{dt} = \sum_{j=1}^{n_i^c} \mathbf{F}_{ij}^c + \mathbf{F}_i^g + \mathbf{F}_i^f \\ I_i \dfrac{d\boldsymbol{\omega}_i}{dt} = \sum_{j=1}^{n_i^c} \mathbf{M}_{tij} + \mathbf{M}_{rij} \end{cases} \tag{A1}$$

where m_i and I_i denote the mass and moment of inertia of particle i, respectively. $\mathbf{U}_i$ and $\boldsymbol{\omega}_i$ are the transitional and angular velocities of particle i, respectively. $\mathbf{F}_{ij}^c$ is the contact force acting on particle i by particle j. $\mathbf{M}_{tij}$ and $\mathbf{M}_{rij}$ are the torques acting on particle i by particle j arising from the tangential force and the rolling friction force, respectively. $\mathbf{F}_i^f$ and $\mathbf{F}_i^g$ are the particle-fluid interaction force and gravity force acting on particle i. $\mathbf{F}_i^g$ equals to zero as the gravity force is dismissed in this study.

The inter-particle rolling torque is calculated by the directional constant torque model proposed by Zhou et al. (1999):

$$\mathbf{M}_r = -\frac{\boldsymbol{\omega}_i - \boldsymbol{\omega}_j}{\left|\boldsymbol{\omega}_i - \boldsymbol{\omega}_j\right|} \mu_r F_n R_r \tag{A2}$$

where $\boldsymbol{\omega}_i$ and $\boldsymbol{\omega}_j$ are the angular velocities of two contacting particles i and j, respectively; $|\boldsymbol{\omega}_i\text{-}\boldsymbol{\omega}_j|$=norm of $\boldsymbol{\omega}_i\text{-}\boldsymbol{\omega}_j$; μ_r is the coefficient of rolling resistance; and R_r=rolling radius defined by $R_r=r_ir_j/(r_i+r_j)$, where r_i and r_j are radii of contacting particles i and j, respectively. In the DEM code, the Hertzian contact law (Mindlin and Deresiewicz, 1953; Renzo and Maio, 2004) with Coulomb's friction law is employed to describe the inter-particle contact behavior.

Governing equations for computational fluid dynamics

The CFD code solves the following continuity equation and locally averaged Navier-Stokes equation accounting for the presence of particles in the fluid.

$$\begin{cases} \dfrac{\partial(n\rho)}{\partial t} + \nabla\cdot(n\rho\mathbf{U}^f) = 0 \\ \dfrac{\partial(n\rho)}{\partial t} + \nabla\cdot(n\rho\mathbf{U}^f\mathbf{U}^f) - n\nabla\cdot(\mu\nabla\mathbf{U}^f) = -\nabla p - \mathbf{f}^p + n\rho\mathbf{g} \end{cases} \tag{A3}$$

where $\mathbf{U}^f$ is the average velocity of a fluid cell. n is the local porosity which is used to account for the particle influence on the fluid computation. p is the fluid pressure, $\mathbf{f}^p$ is the average particle-fluid interaction force per unit volume, ρ and μ is the fluid density and viscosity, respectively. The fluid viscosity is the property of a fluid to be resistant to flow. Fluids with a high viscosity are more resistant to flow. The particle-fluid interaction force ($\mathbf{F}_i^f$) in Eq (A1) is the fluid force acting on a single particle. The average particle-fluid interaction force ($\mathbf{f}^p$) in Eq (A3) is the reaction force of the $\mathbf{F}_i^f$ within the volume of a fluid cell. As gravity is not considered in this study, the gravitational component in this equation equals to zero.

Governing equations for particle-fluid interaction forces

In this study, the particle-fluid interaction forces, including the drag force ($\mathbf{F}^d$), pressure gradient force ($\mathbf{F}^p$) and viscous force ($\mathbf{F}^v$), are considered as shown in Eq. A4 (Hu et al., 2018).

$$\mathbf{F}^f = \mathbf{F}^d + \mathbf{F}^p + \mathbf{F}^v \tag{A4}$$

The drag force is adopted from the expression proposed by Di Felice (1994), which is applicable for a dense granular regime and valid for a wide range of Reynolds numbers:

$$\begin{cases} \mathbf{F}^d = \frac{1}{8} C_d \rho \pi d_p^2 (\mathbf{U}^f - \mathbf{U}^p) \left| \mathbf{U}^f - \mathbf{U}^p \right| n^{1-\chi} \\ C_\mathrm{d} = \left(0.63 + \frac{4.8}{\sqrt{\mathrm{Re}_p}} \right)^2 \\ \mathrm{Re}_p = \frac{n \rho d_p \left| \mathbf{U}^f - \mathbf{U}^p \right|}{\mu} \\ \chi = 3.7 - 0.65 \exp[-\frac{(1.5 - \log_{10} \mathrm{Re}_p)^2}{2}] \end{cases} \tag{A5}$$

where d_p is the diameter of particles and C_d is the particle-fluid drag coefficient for a single spherical particle that depends on the Reynolds number of the particle (Re_p). χ in Eq. A5 is a correlation function that modifies the coefficient of drag force accounting for the presence of other particles in the system.

The pressure gradient force ($\mathbf{F}^p$) and viscous force for a single particle are formulated by Eqs. (A6) and (A7), respectively (Zhou et al., 2010):

$$\mathbf{F}^p = -V_p \nabla p \tag{A6}$$

$$\mathbf{F}^v = -V_p \nabla \cdot \boldsymbol{\tau} \tag{A7}$$

where $\boldsymbol{\tau}$ is the viscous stress tensor which describes the friction between the fluid and the surface of particles.

References

Amir Z, Brij M. Flow of dispersed particles through porous media-Deep bed filtration. Journal of Petroleum Science and Engineering. 2009, 69:71-88.

Alem A, Ahfir ND, Elkawafi A, Wang HQ. Hydraulic Operating Conditions and Particle Concentration Effects on Physical Clogging of a Porous Medium. Transport in Porous Media. 2015, 106:303-321.

Bacchin P, Derekx Q, Veyret D, Glucina K, Moulin P. Clogging of microporous channels networks: role of connectivity and tortuosity. Microfluid Nanofluid. 2014, 17:85-96.

Bendahmane F, Marot D, Alexis A. Experimental parametric study of suffusion and backward erosion. Journal of Geotechnical and Geoenvironmental Engineering. 2008, 134(1):57-67.

Benamar A, Santos RNC, Bennabi A, Karoui T. Suffusion evaluation of coarse-graded soils from Rhine dikes. Acta Geotechnica. 2019, 14(3):815-823.

Burenkova, V.V. Assessment of Suffusion in Non-Cohesive and Graded Soils. In: Brauns, J., Schuler, U. and Heibum, M., Eds., Proceedings of the 1st International Conference "Geo-Filters", Filters in Geotechnical Engineering, Balkema, 1993, 357-360.

Chang DS, Zhang LM. Critical Hydraulic Gradients of Internal Erosion under Complex Stress States. J. Geotech. Geoenvironmental. Eng. 2013, 139(9), 1454-1467.

Chang DS. Internal erosion and overtopping erosion of earth dams and landslide dams. PhD thesis. 2012. Hong Kong University of Science and Technology.

Goldsztein GH. Volume of suspension that flows through a small orifice before it clogs. SIAM J. APPL. MATH, 2005, 66(1):228-236.

Goniva C, Kloss C, Deen NG et al. Influence of rolling friction on single spout fluidized bed simulation. Particuology. 2012, 10:582-591.

Han G, Kwon TH, Lee JY, Kneafsey TJ. Depressurization-induced fines migration in sediments containing methane hydrate: X-Ray computed tomography imaging experiments. Journal of Geophysical Research: Solid Earth. 123, 2539-2558.

Hicher P-Y. Modelling the impact of particle removal on granular material behavior. Géotechnique. 2013, 63(2):118-128.

Hu Z, Zhang YD, Yang ZX. Suffusion-induced deformation and microstructural change of granular soils: a coupled CFD-DEM study. Acta Geotechnica. 2019, 14:795-814.

Indraratna B, Raut A, Khabbaz H. Constriction-based retention criterion for granular filter design. Journal of Geotechnical and Geoenvironmental Engineering. 2007, 133(3):266-276.

Indraratna B, Israr J, Rujikiatkamjorn C. Geometrical Method for Evaluating the Internal Instability of Granular Filters Based on Constriction Size Distribution. Journal of Geotechnical and Geoenvironmental Engineering. 2015, 141(10):04015045.

Israr J, Indraratna B. Study of critical hydraulic gradients for seepage-induced failures in granular soils. Journal of Geotechnical and Geoenvironmental Engineering. 2019, 145(7): 04019025.

Jasak H, Jemcov A, Tukovic Z. OpenFOAM: A C++ library for complex physics simulations. Proc., Int. Workshop on Coupled Methods in Numerical Dynamics. Dubrovnik, Croatia. 2007, 1000.

Ke L, Takahashi A. Drained monotonic responses of suffusional cohesionless soils. Journal of Geotechnical and Geoenvironmental Engineering. 2015, 141(8): 04015033.

Kawano K, Shire T, O'Sullivan C. Coupled particle-fluid simulations of the initiation of suffusion. Soils and Foundations. 2018, 58(4):972-985.

Kloss C, Goniva C, Hager A et al. Models, algorithms and validation for opensource DEM and CFD-DEM. Prog. Comput. Fluid. Dyn. Int. J. 2012, 12:140-152.

Kezdi, A. Soil physics-selected topics. Elsevier Scientific Publishing Co. Amsterdam, 1979.

Li M. Seepage induced instability in widely graded soils. Ph.D. thesis, Univ. of British Columbia, Vancouver, BC, Canada, 2008.

Marot D, Regazzoni PL, Wahl T. Energy-based method for providing soil surface erodibility rankings. Journal of Geotechnical and Geoenvironmental Engineering. 2011, 137(12):1290-1293.

Moffat R, Fannin RJ, Garner SJ. Spatial and temporal progression of internal erosion in cohesionless soil. Canadian Geotechnical Journal. 2011, 48(3):399-412.

Minh NH, Cheng YP, Thornton C. Strong force networks in granular mixtures. Granular Matter. 2014, 16:69-78.

Mindlin RD, Deresiewicz H. Elastic spheres in contact under varying oblique forces. Transactions of ASME, Series E. Journal of Applied Mechanics. 1953, 20:327-344.

Nguyen CD, Nadia B, Edward A, Luc S, Pierre P. Experimental investigation of microstructural changes in soils eroded by suffusion using X-ray tomography. Acta Geotechnica. 2019. https://doi.org/10.1007/s11440-019-00787-w.

Nguyen TT and Indraratna B. A coupled CFD-DEM approach to examine the hydraulic critical state of soil under increasing hydraulic gradient. ASCE International Journal of Geomechanics. 2020(a), 20(9):04020138-1:15.

Nguyen TT, Indraratna B. The role of particle shape on hydraulic conductivity of soils based on Kozeny-Carman approach. Géotechnique Letters. 2020(b), 10(3):1-15.

Reddi LN, Xiao M, Hajra MG, Lee IM. Physical clogging of soil filters under constant flow rate versus constant head. Canadian Geotechnical Journal. 2005, 42:804-811.

Renzo AD, Maio FPD. Comparison of contact-force models for the simulation of collisions in DEM-based granular flow codes. Chemical Engineering Science. 2004, 59(3):525-541.

Santos RNC, Caldeira LMMS, NEVES E MD. Experimental study on crack filling by upstream fills in dams. Géotechnique. 2015, 65(3), 218-230.

Skempton AW, Brogan J. M. Experiments on piping in sandy gravels. Géotechnique. 1994, 44(3): 449-460.

Sibille L, Marot Di, Sail Y. A description of internal erosion by suffusion and induced settlements on cohesionless granular matter. Acta Geotechnica. 2015, 10:735-748.

Sterpi D. Effects of the erosion and transport of fine particles due to seepage flow. International Journal of Geomechanics. 2003, 3(1):111-122.

Shire T, O'Sullivan C, Hanley KJ, Fannin RJ. Fabric and effective stress distribution in internally unstable soils. Journal of Geotechnical and Geoenvironmental Engineering. 2014, 140(12):04014072.

Shire T, O'Sullivan C. Constriction size distributions of granular filters: a numerical study. Géotechnique. 2016, 66(10):826-839.

Scheidegger, AE. The Physics of Flow Through Porous Media. Toronto: University of Toronto Press. 1960.

Valdes JR, Santamarina JC. Particle transport in a nonuniform flow field: retardation and clogging. Applied Physics Letters. 2007, 90:244101.

Valdes JR, Liang SH. Stress-controlled filtration with compressible particles. Journal of Geotechnical and Geoenvironmental Engineering. 2006, 132(7):861-868.

Wang J. Gutierrez M. Discrete element simulations of direct shear specimen scale effects. Géotechnique. 2010, 60(5):395-409.

Wautier A, Bonelli S, Nicot F. Flow impact on granular force chains and induced instability. 2018. Pysical review E. 98, 042909.

Wautier A, Bonelli S, Nicot F. DEM investigations of internal erosion: Grain transport in the light of micromechanics. International Journal for Numerical and Analytical Methods in Geomechanics. 2019, 43:339-352.

Yang Y, Cheng YM, Sun QC. The effects of rolling resistance and non-convex particle on the mechanics of the undrained granular assembles in 2D. Powder Technology. 2017, 318:528-542.

Yang J, Yin Z-Y, Laouafa F, Hicher P-Y. Internal erosion in dike-on-foundation modeled by a coupled hydro-mechanical approach. International Journal for Numerical and Analytical Methods in Geomechanics. 2019, 43(3):663-683.

Yang J, Yin Z-Y, Laouafa F, Hicher P-Y. Hydro-mechanical modeling of granular soils considering internal erosion. Canadian Geotechnical Journal. 2020, 57(2): 157-172.

Yin Z-Y, Zhao J, Hicher P-Y. A micromechanics-based model for sand-silt mixtures. International Journal of Solids and Structures. 2014, 51(6):1350-1363.

Yin Z-Y, Huang HW, Hicher P-Y. Elastoplastic modeling of sand-silt mixtures. Soils and Foundations. 2016, 56(3):520-532.

Zamani A, Maini B. Flow of dispersed particles through porous media — Deep bed filtration. Journal of Petroleum Science and Engineering. 2009, 69:71-88.

Zheng Xi-lai, Shan Bei-bei, Chen L, Sun Yun-wei, Zhang Shu-hui. Attachment-detachment dynamics of suspended particle in porous media: Experiment and modeling. Journal of Hydrology. 2014, 511:199-204.

Zhang FS, Li M, Peng M, Chen C, Zhang L. Three-dimensional DEM modeling of the stress-strain behavior for the gap-graded soils subjected to internal erosion. Acta Geotechnica. 2019, 14, 487-503.

Zhao J, Shan T. Coupled CFD-DEM simulation of fluid-particle interaction in geomechanics. Powder Technology. 2013, 239, 248-258.

Zhao T, Utili S, Crosta GB. Rockslide and impulse wave modelling in the Vajont reservoir by

DEM-CFD analyses. Rock Mechanics and Rock Engineering 2016, 49, 2437-2456.

Zhou YC, Wright BD, Yang RY et al. Rolling friction in the dynamic simulation of sandpile formation. Phys A Stat Mech Appl. 199, 269:536-553.

Tables

Table 1 Simulation program and the number of particles in each sample

Simulation identity	Fine faction, F_c (%)	Suspension concentration, C (g/L)	Hydraulic gradient, i	No. of total particles	No. of coarse particles	No. of fine particles
FC15C0L	15	0	0.1	27287	697	26590
FC15C30L		30	0.1			
FC15C60L		60	0.1			
FC15C0H		0	0.25			
FC15C30H		30	0.25			
FC15C60H		60	0.25			
FC35C0L	35	0	0.1	55203	479	54724
FC35C30L		30	0.1			
FC35C60L		60	0.1			
FC35C0H		0	0.25			
FC35C30H		30	0.25			
FC35C60H		60	0.25			

Table 2 Summary of model parameters

	Model parameters	Values for the validation model	Values for the model with suspension flow
Physical model	Sample dimensions $L \times W \times H$ (mm)	13×13×13	13×13×26
	Simulation time (s)	40.0	15.0
CFD	Cells	5×5×6	5×5×12
	Fluid viscosity, μ (Pa·s)	1×10^{-3}	1×10^{-3}
	Density, ρ (kg/m^3)	1000	1000
	Time step (s)	1×10^{-4}	1×10^{-4}
DEM	Elastic modulus, E (Pa)	7×10^{9}	7×10^{9}
	Poisson's ratio, v	0.3	0.3
	Coefficient of Restitution, e	0.7	0.7
	Friction coefficient, μ_f	0.5	0.5
	Rolling friction coefficient, μ_r	0.1	0.1
	Time step (s)	5×10^{-7}	5×10^{-7}

Caption of Figures

Figure 1 Grain size distribution of the soils in this study and the experiment of Chang (2012)

Figure 2 Erosion behavior of the sample with F_c=35%: (a) cumulative eroded soil weight percentage under p'=50 and 200 kPa; (b) sample deformations under p'=50 kPa; (c) sample deformations under p'=200 kPa

Figure 3 Assessment of internal stability for the samples with F_c=15% and 35% by Burenkova method

Figure 4 Model setup

Figure 5 Simulation results for the samples with F_c=15% under different hydraulic gradient and suspension concentration: (a) cumulative eroded soil weight percentage; (b) vertical strain; (c) transverse strain

Figure 6 Cumulative eroded soil weight percentage in the case of i=0.25 and F_c=15% under different concentrations and rolling friction

Figure 7 Simulation results for the samples with F_c=35% under different hydraulic gradient and suspension concentration: (a) cumulative eroded soil weight percentage; (b) vertical strain; (c) transverse strain

Figure 8 Erosion rate in terms of mass percentage for the samples with (a) F_c=15% and (b) F_c=35% under different suspension concentrations (C) and hydraulic gradients (i)

Figure 9 Distribution of the fine fraction after erosion along the height of the sample with (a) F_c=15% (b) F_c=35%

Figure 10 Evolution of the hydraulic conductivity for the sample with (a) F_c=15% and (b) F_c=35% (k_0 of the sample with F_c=15% and 35% are 3.6×10^{-4}cm/s and 1.8×10^{-4}cm/s, respectively)

Figure 11 Comparison of the tortuosity (τ) calculated by the approach of this study with that of Nguyen and Indraratna (2020(b)) for the samples with (a) F_c=15% and (b) F_c=35%

Figure 12 Interaction between fine migration and fluid flow at the (a) initial time and (b) end of the simulation for the sample with F_c=15% and (c) initial time and (d) end of the simulation for the sample with F_c=35% under i=0.25 and C=30 g/L

Figure 13 Evolution of the local packing configuration and constriction size distribution for the (a) erosion area and (b) clogging area

Figure 14 Coordination number and number density of the fine particles in the cluster and the entire sample

Figure 15 Relationship between the constriction size distribution and the retention ratio for (a) region A; (b) region B

Figure 16 Assessment of the retention ratio based on P_{mean} and concentration (normalized by the average concentration of the eight sub-zones)

Figure 17 Relationship between the average particle-fluid interaction force during erosion and migration distance for the suspension particles in the case of Fc=15%, C=70 g/L, and i=0.25 (a) at the end of erosion; (b) during internal erosion

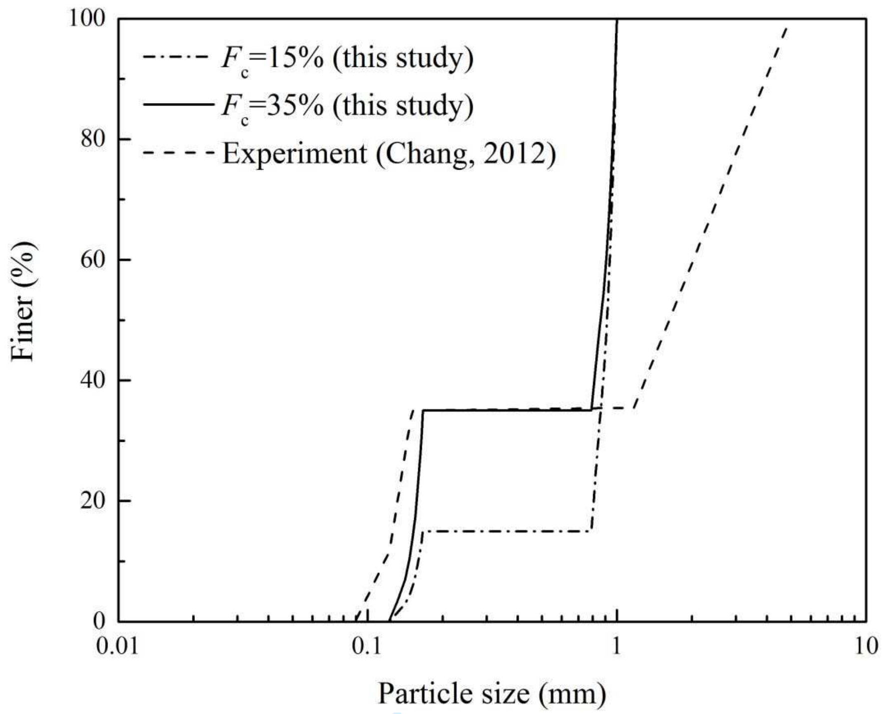

Figure 1 Grain size distribution of the soils in this study and the experiment of Chang (2012)

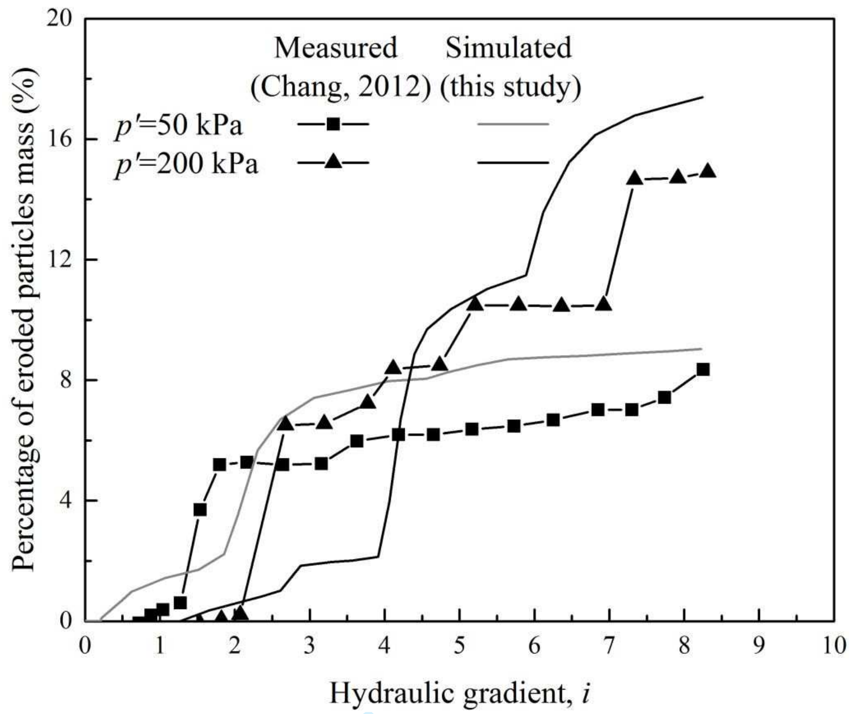

Measured (Chang, 2012)
Simulated (this study)
p′=50 kPa
p′=200 kPa
Percentage of eroded particles mass (%)
Hydraulic gradient, i
0
4
8
12
16
20
0
1
2
3
4
5
6
7
8
9
10

(a)

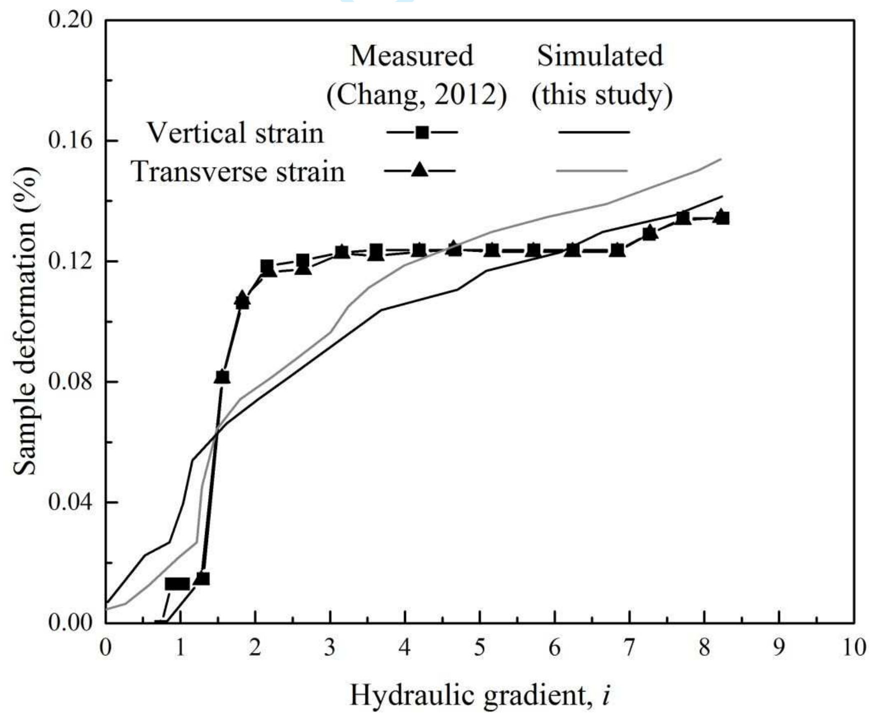

Measured (Chang, 2012)
Simulated (this study)
Vertical strain
Transverse strain
Sample deformation (%)
Hydraulic gradient, i
0.00
0.04
0.08
0.12
0.16
0.20
0
1
2
3
4
5
6
7
8
9
10

(b)

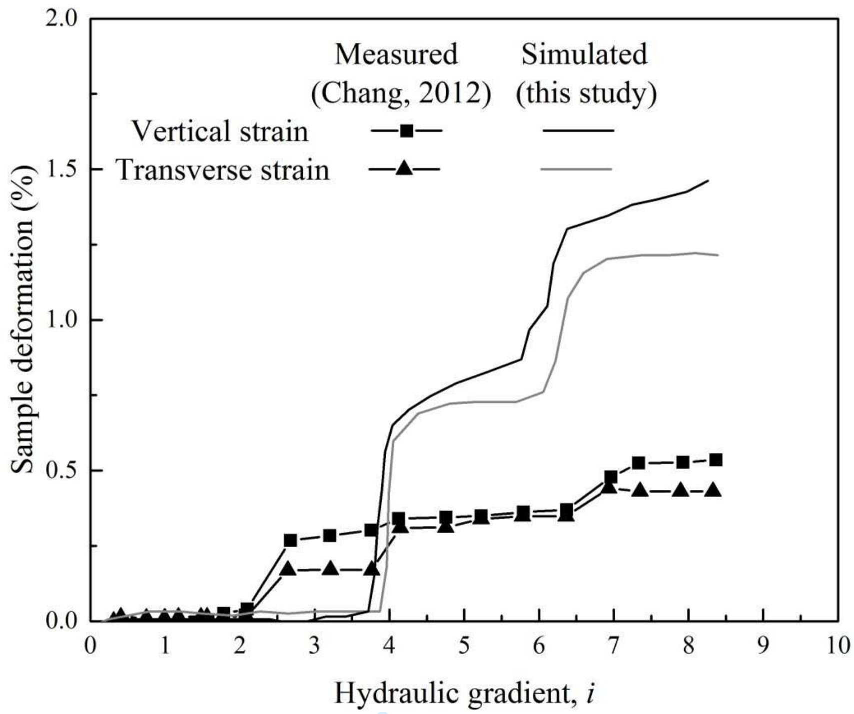

(c)

Figure 2 Erosion behavior of the sample with F_c=35%: (a) cumulative eroded soil weight percentage under p'=50 and 200 kPa; (b) sample deformations under p'=50 kPa; (c) sample deformations under p'=200 kPa

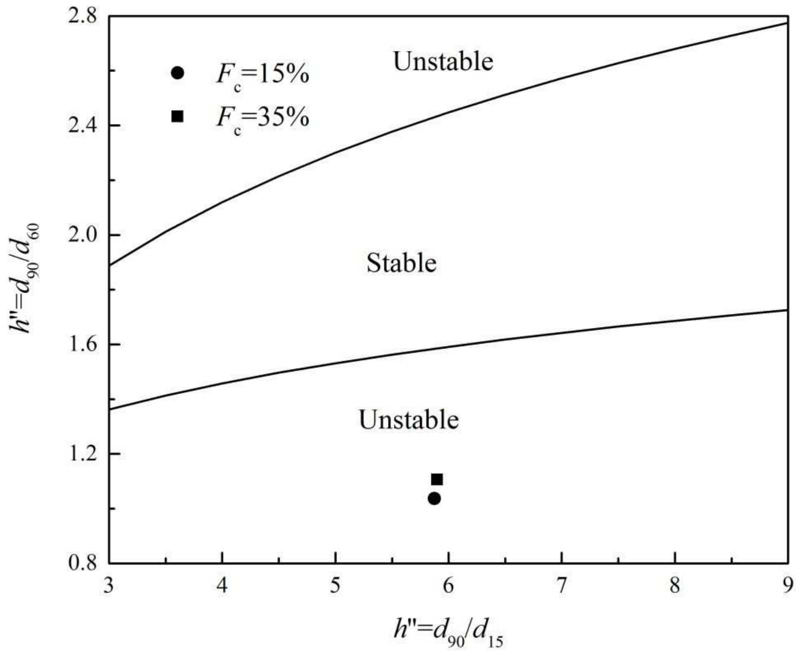

Figure 3 Assessment of internal stability for the samples with F_c=15% and 35% by Burenkova method

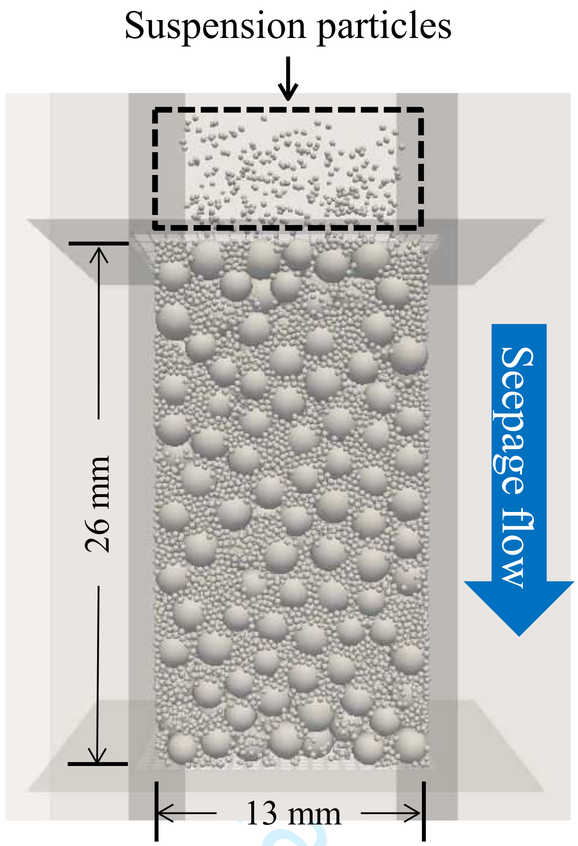

Figure 4 Model setup

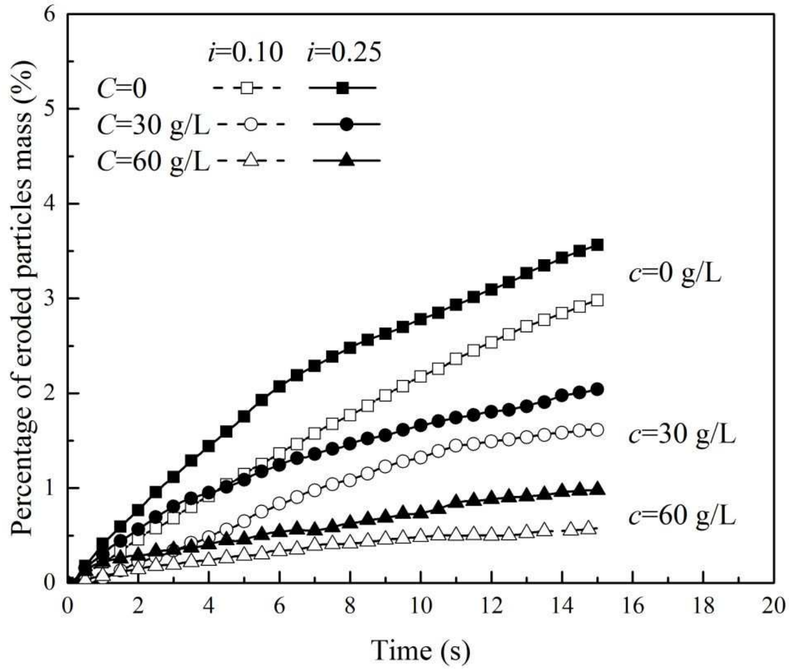

Percentage of eroded particles mass (%)
Time (s)
i=0.10
i=0.25
C=0
C=30 g/L
C=60 g/L
c=0 g/L
c=30 g/L
c=60 g/L

(a)

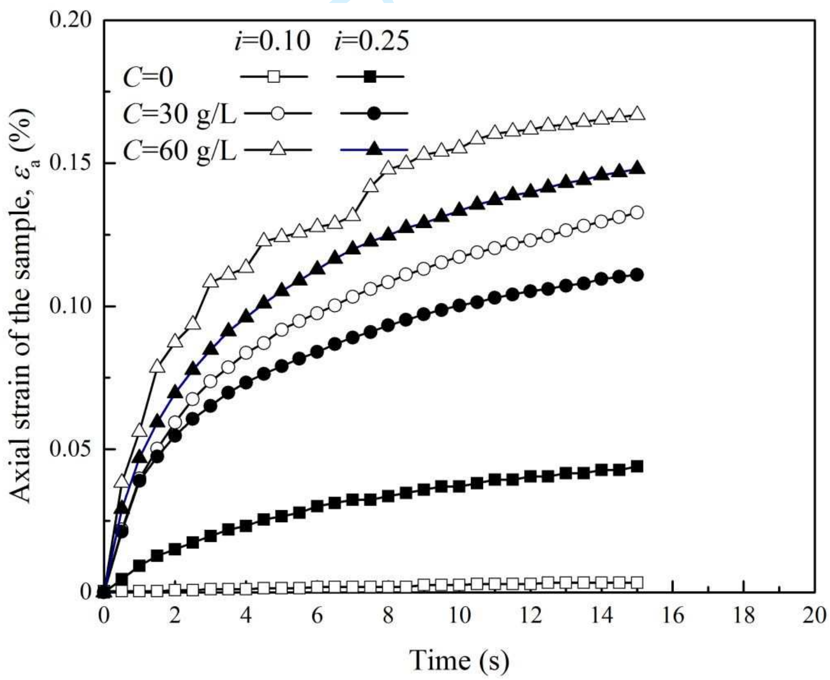

Axial strain of the sample, ε_a (%)
Time (s)
i=0.10
i=0.25
C=0
C=30 g/L
C=60 g/L

(b)

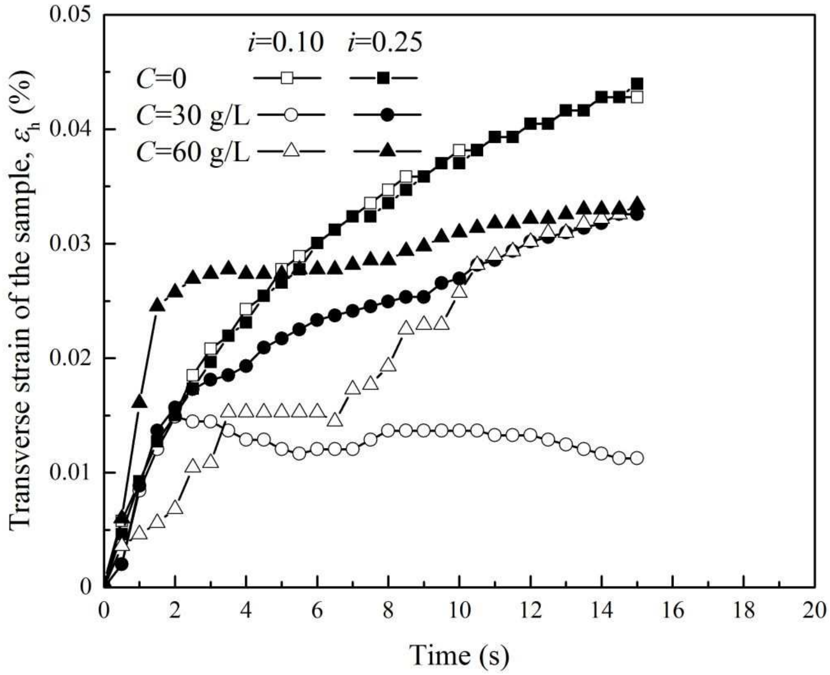

(c)

Figure 5 Simulation results for the samples with F_c=15% under different hydraulic gradient and suspension concentration: (a) cumulative eroded soil weight percentage; (b) vertical strain; (c) transverse strain

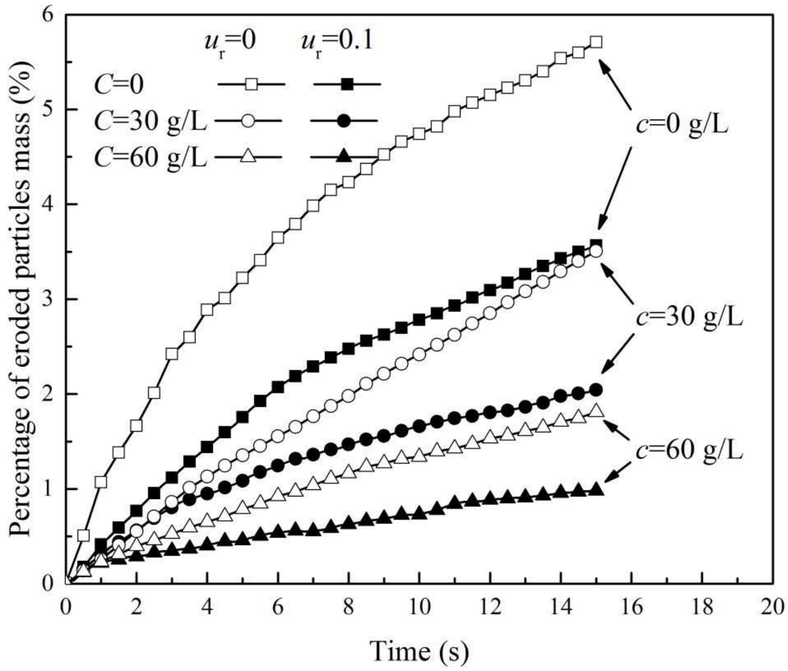

Figure 6 Cumulative eroded soil weight percentage in the case of i=0.25 and F_c=15% under different concentrations and rolling friction

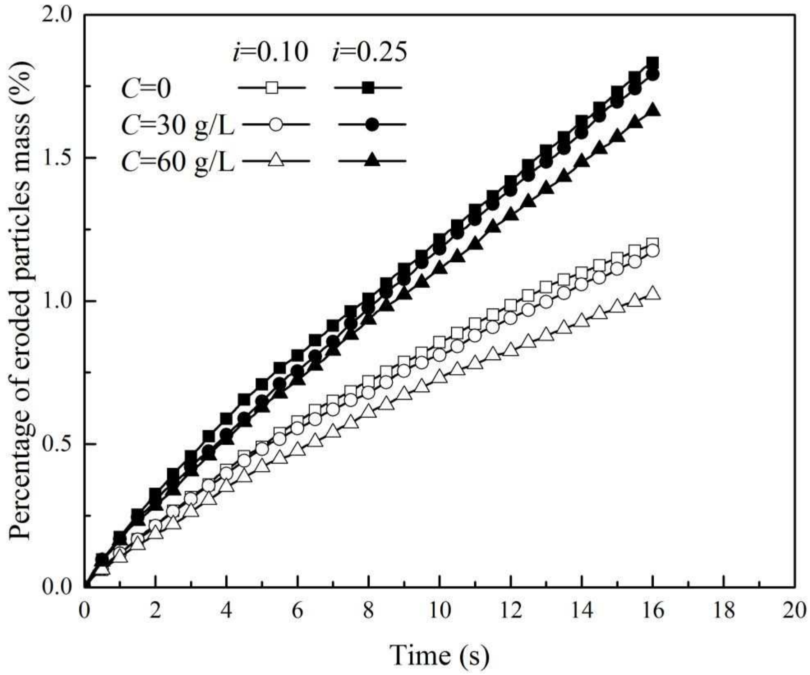

i=0.10 i=0.25
C=0
C=30 g/L
C=60 g/L
Percentage of eroded particles mass (%)
Time (s)
0.0
0.5
1.0
1.5
2.0
0 2 4 6 8 10 12 14 16 18 20

(a)

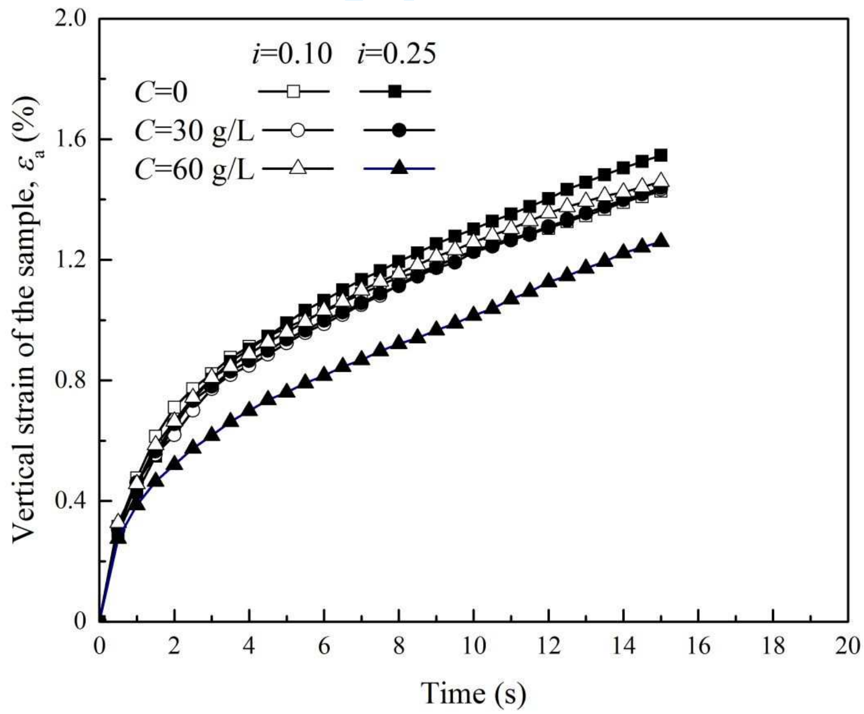

i=0.10 i=0.25
C=0
C=30 g/L
C=60 g/L
Vertical strain of the sample, ε_a (%)
Time (s)
0
0.4
0.8
1.2
1.6
2.0
0 2 4 6 8 10 12 14 16 18 20

(b)

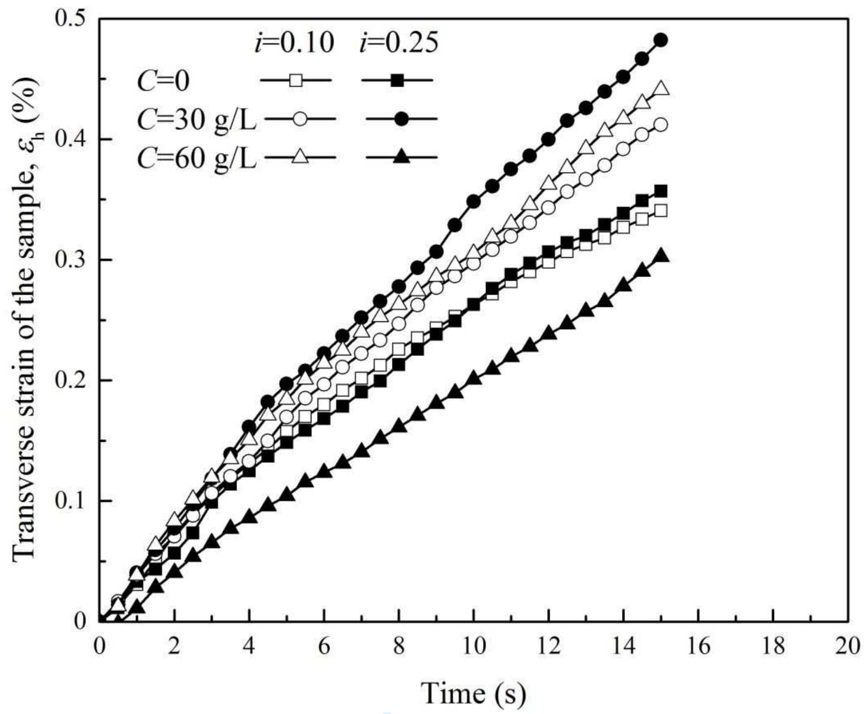

(c)

Figure 7 Simulation results for the samples with F_c=35% under different hydraulic gradient and suspension concentration: (a) cumulative eroded soil weight percentage; (b) vertical strain; (c) transverse strain

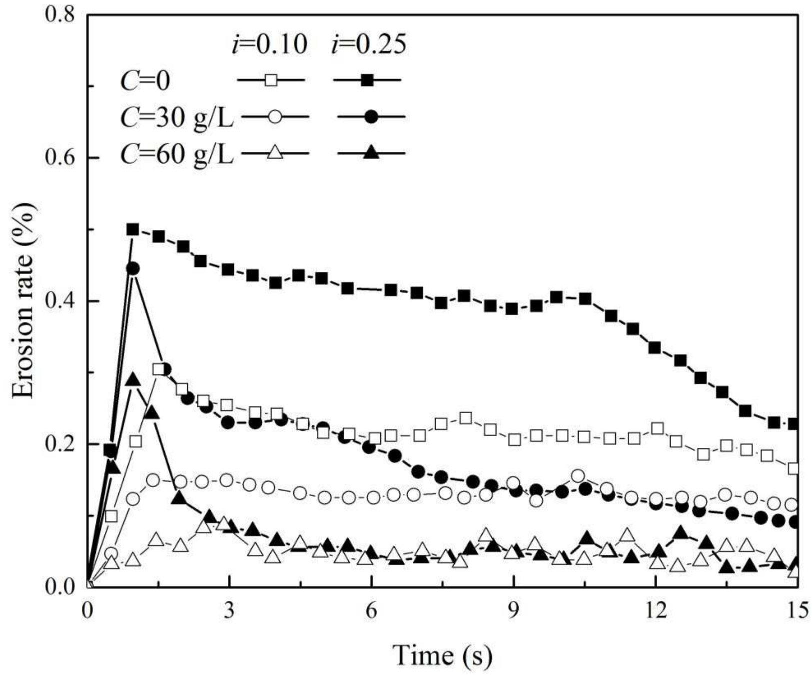

(a)

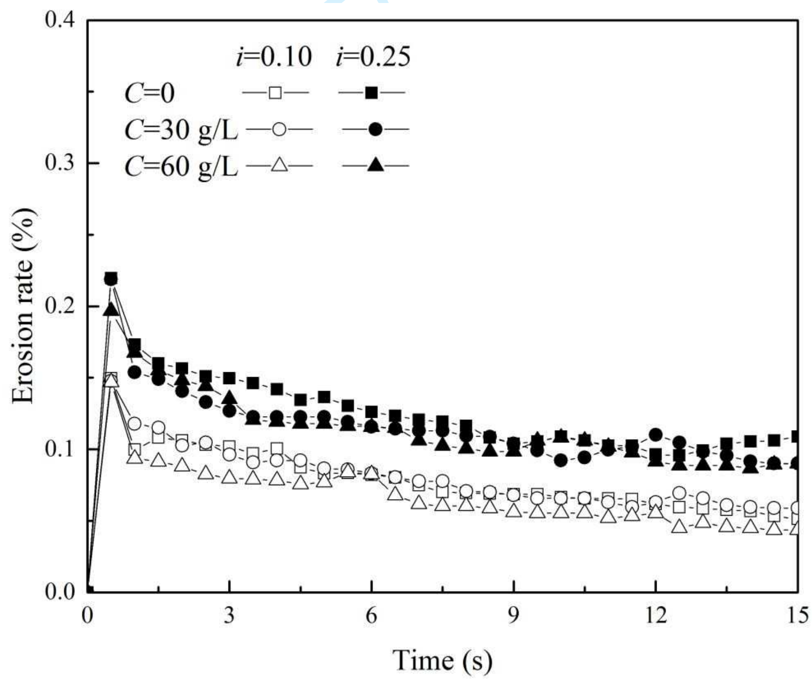

(b)

Figure 8 Erosion rate in terms of mass percentage for the samples with (a) F_c=15% and (b) F_c=35% under different suspension concentrations (C) and hydraulic gradients (i)

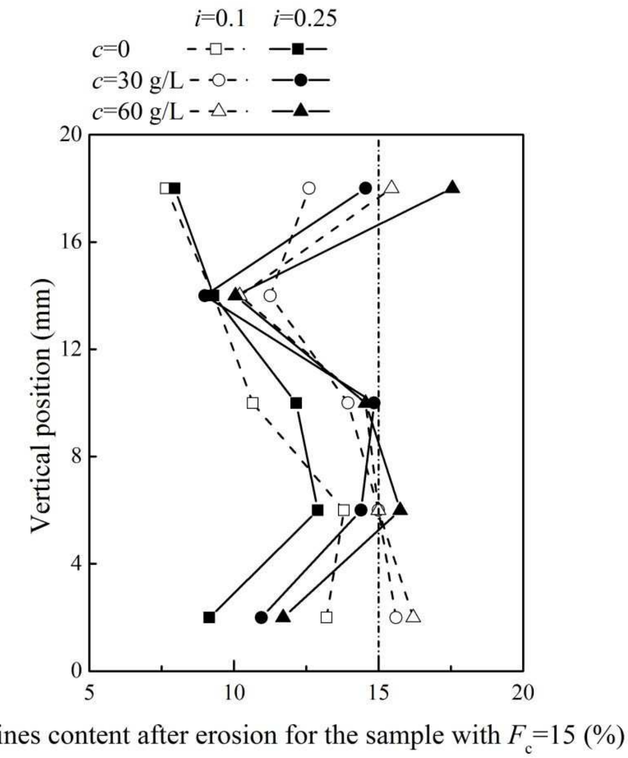

(a)

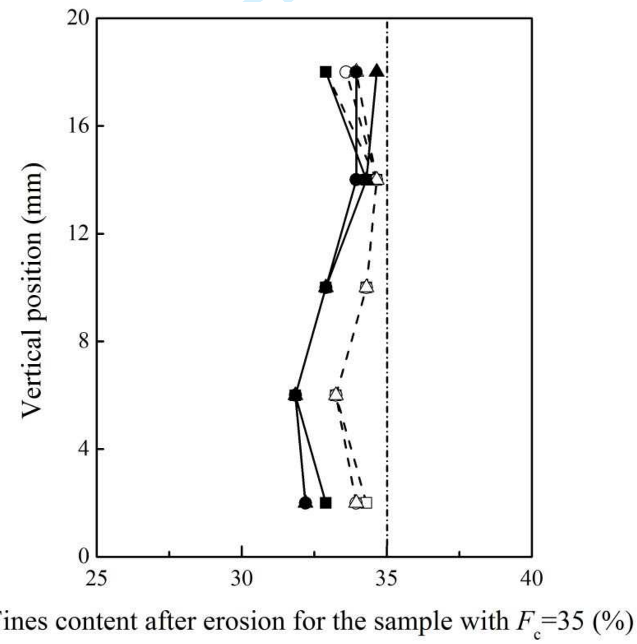

(b)

Figure 9 Distribution of the fine fraction after erosion along the height of the sample with (a) F_c=15% (b) F_c=35%

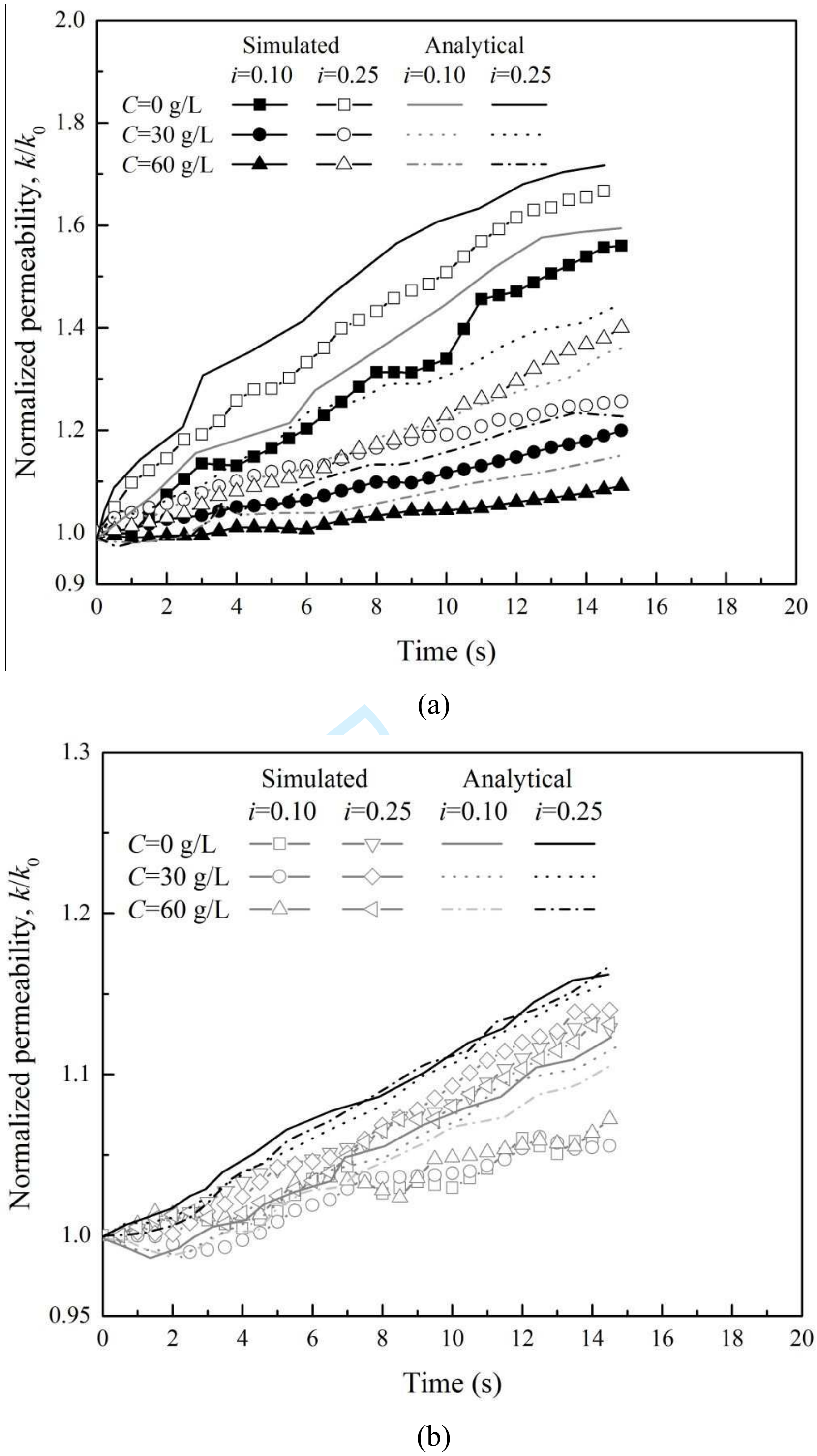

Figure 10 Evolution of the hydraulic conductivity for the sample with (a) F_c=15% and (b) F_c=35% (k_0 of the sample with F_c=15% and 35% are 3.6×10^{-4}cm/s and 1.8×10^{-4}cm/s, respectively)

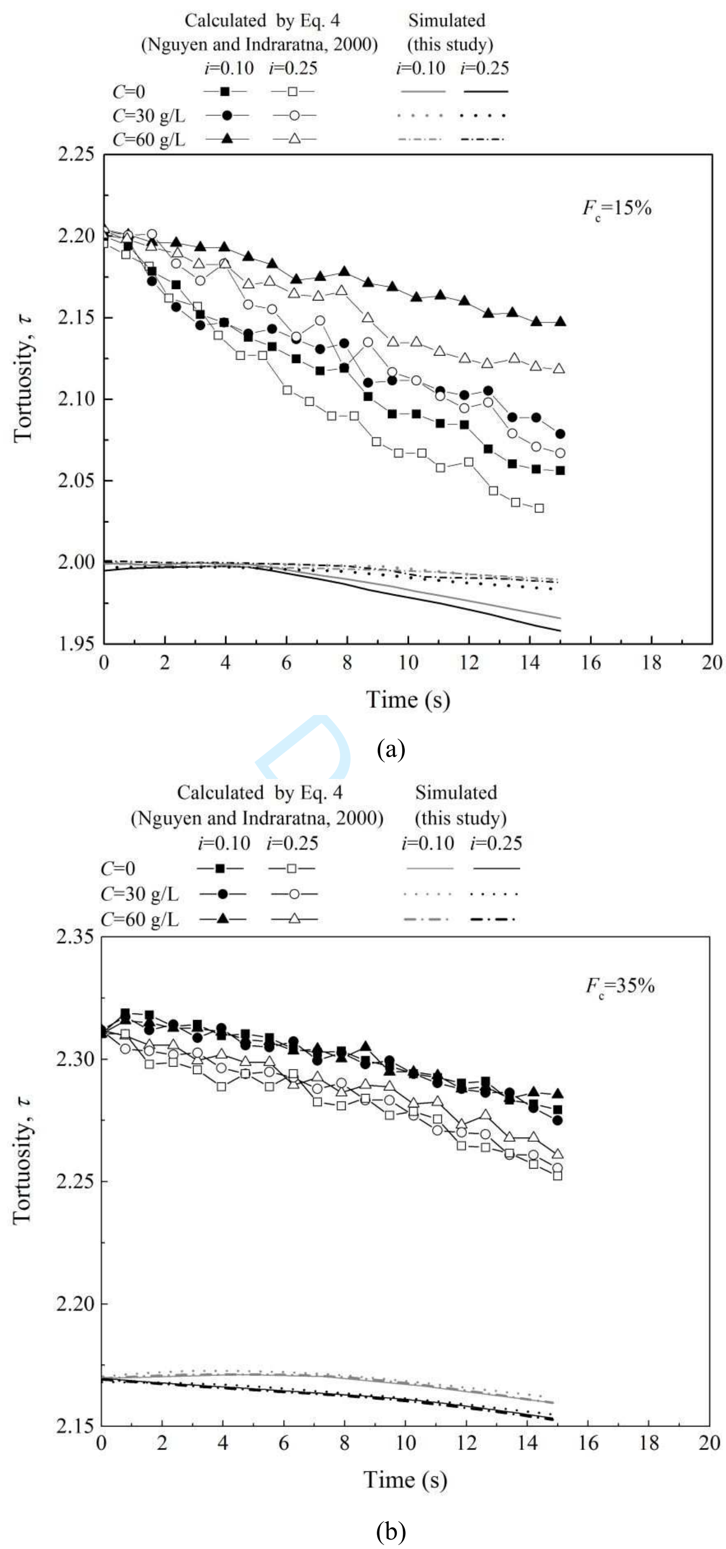

Figure 11 Comparison of the tortuosity (τ) calculated by the approach of this study with that of Nguyen and Indraratna (2020(b)) for the samples with (a) F_c=15% and (b) F_c=35%

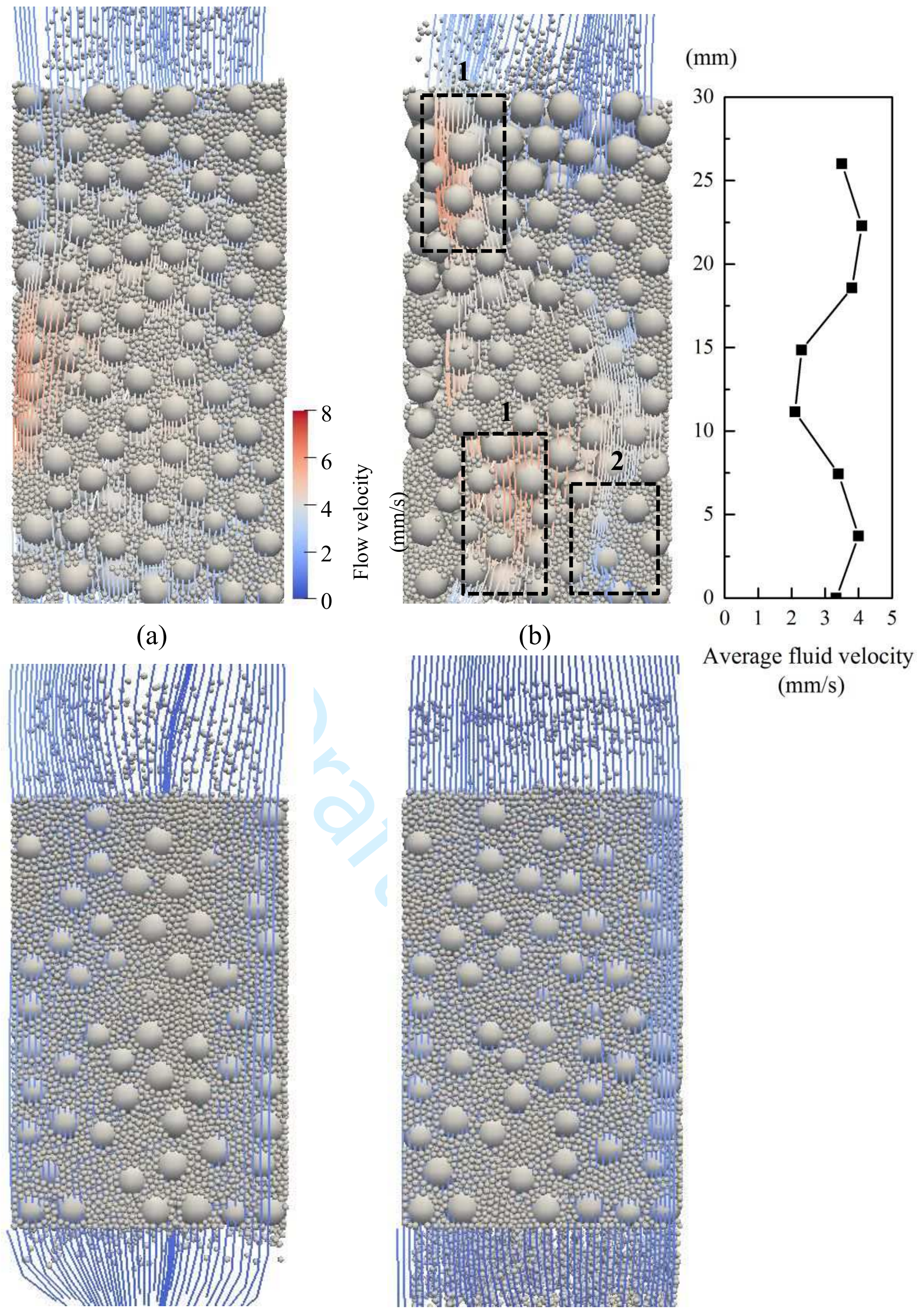

Figure 12 Interaction between fine migration and fluid flow at the (a) initial time and (b) end of the simulation for the sample with F_c=15% and (c) initial time and (d) end of the simulation for the sample with F_c=35% under i=0.25 and C=30 g/L

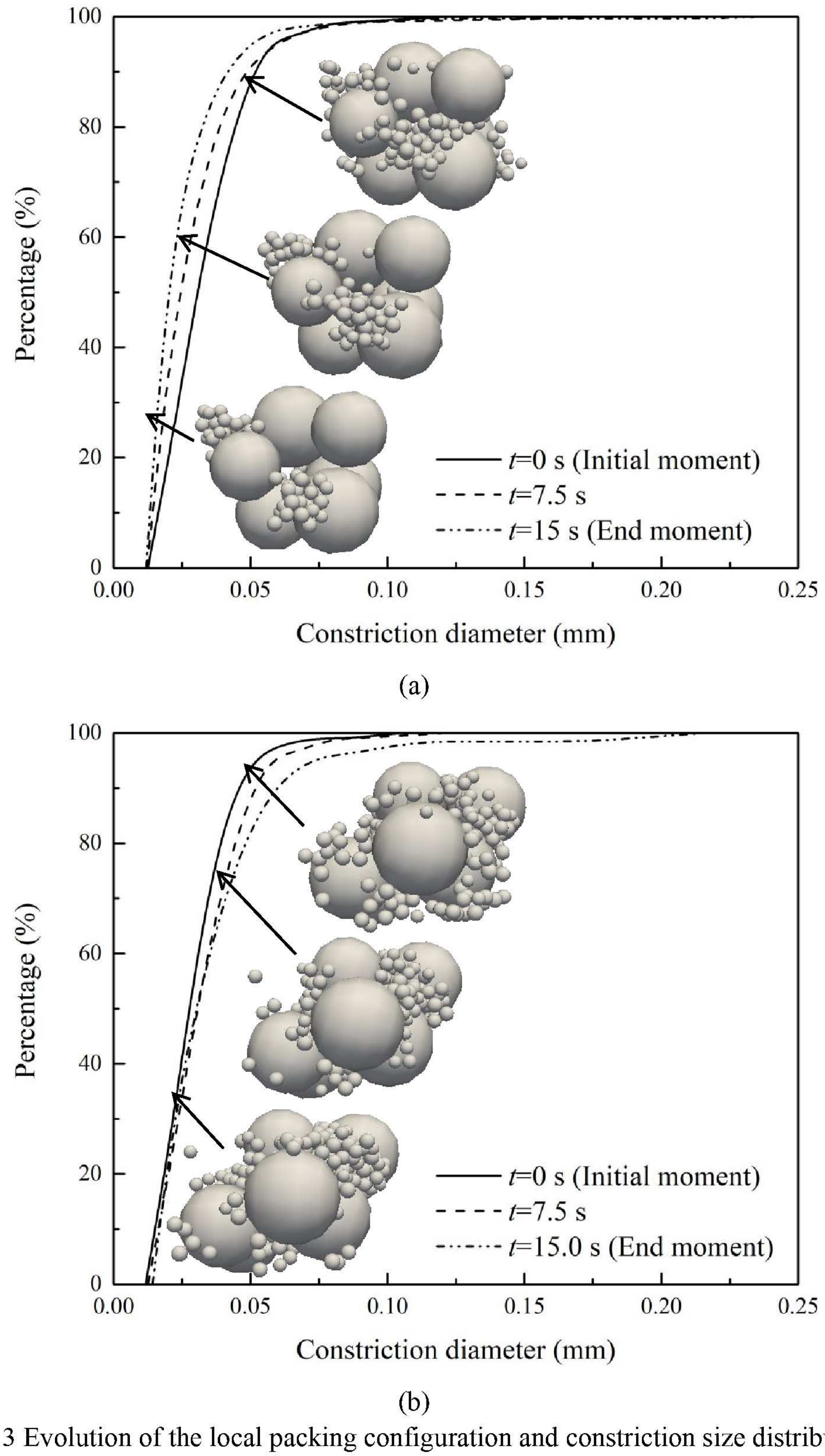

(b)

Figure 13 Evolution of the local packing configuration and constriction size distribution for the (a) erosion area and (b) clogging area

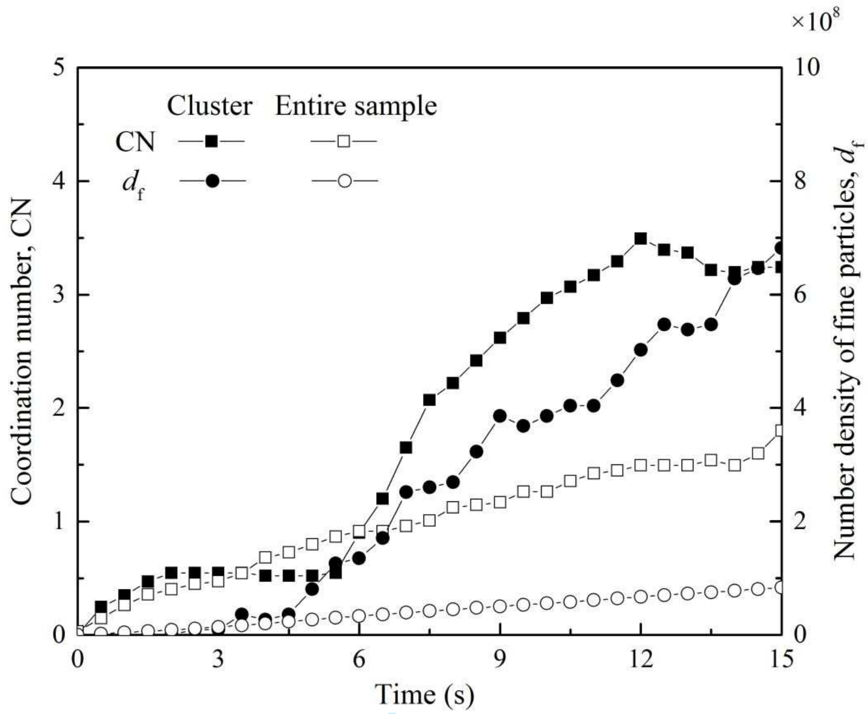

Figure 14 Coordination number and number density of the fine particles in the cluster and the entire sample

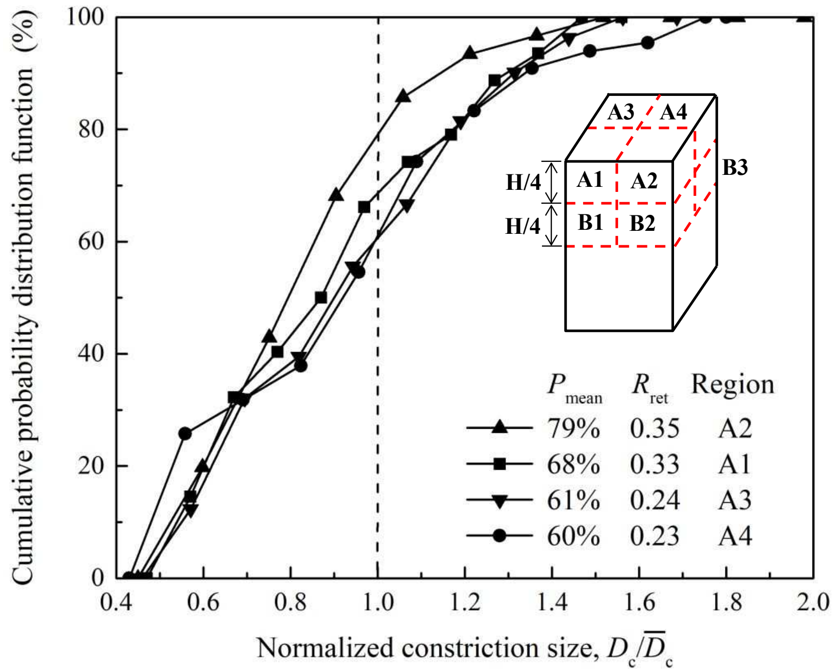

(a)

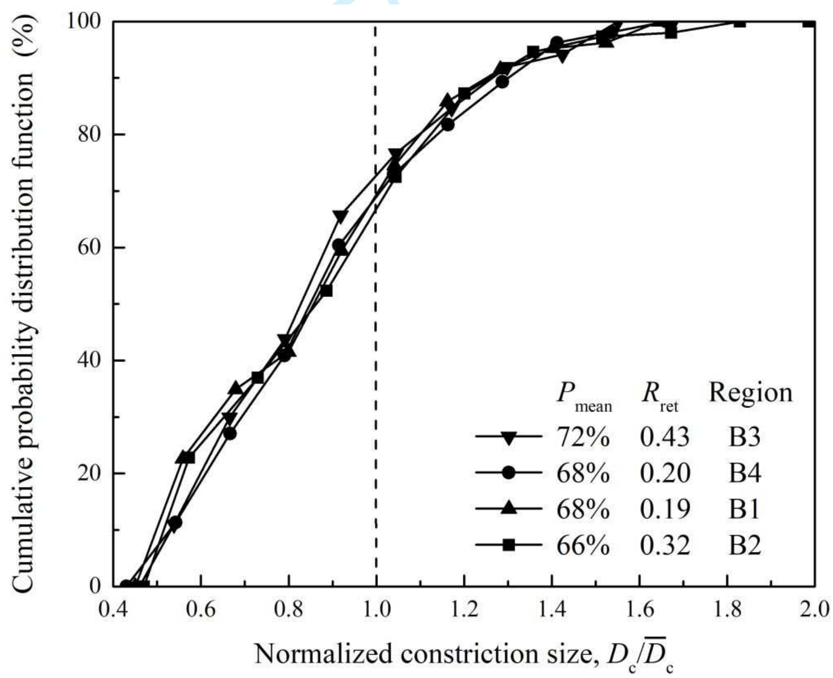

(b)

Figure 15 Relationship between the constriction size distribution and the retention ratio for (a) region A; (b) region B

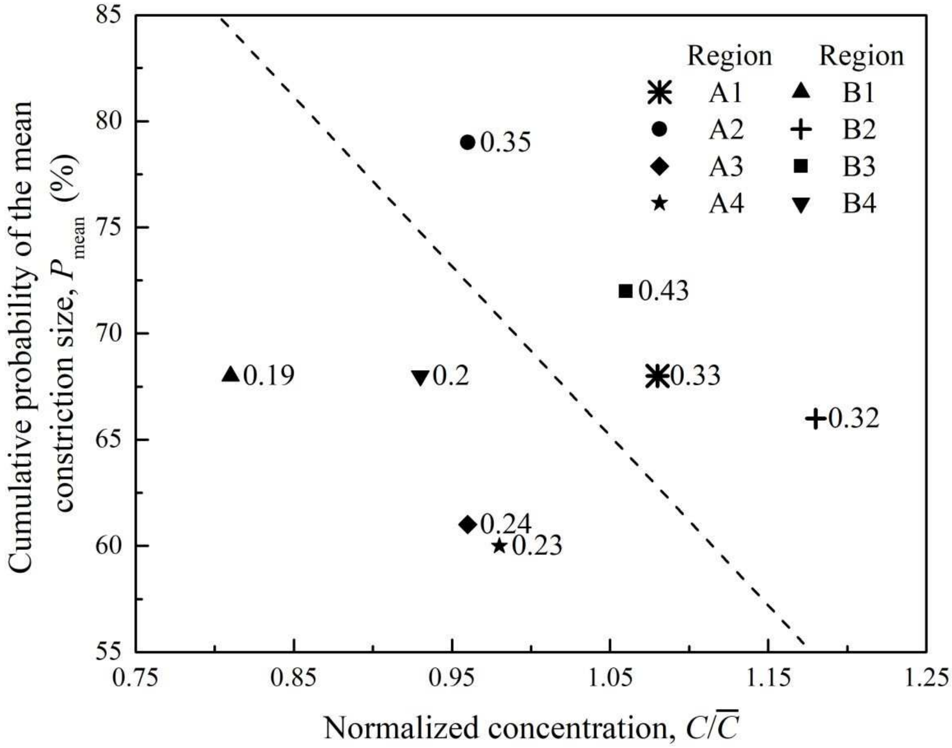

Figure 16 Assessment of the retention ratio based on P_{mean} and concentration (normalized by the average concentration of the eight sub-zones)

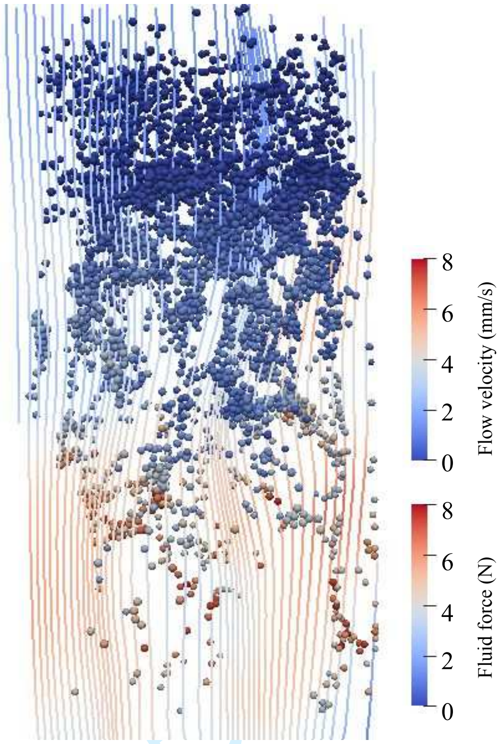

(a)

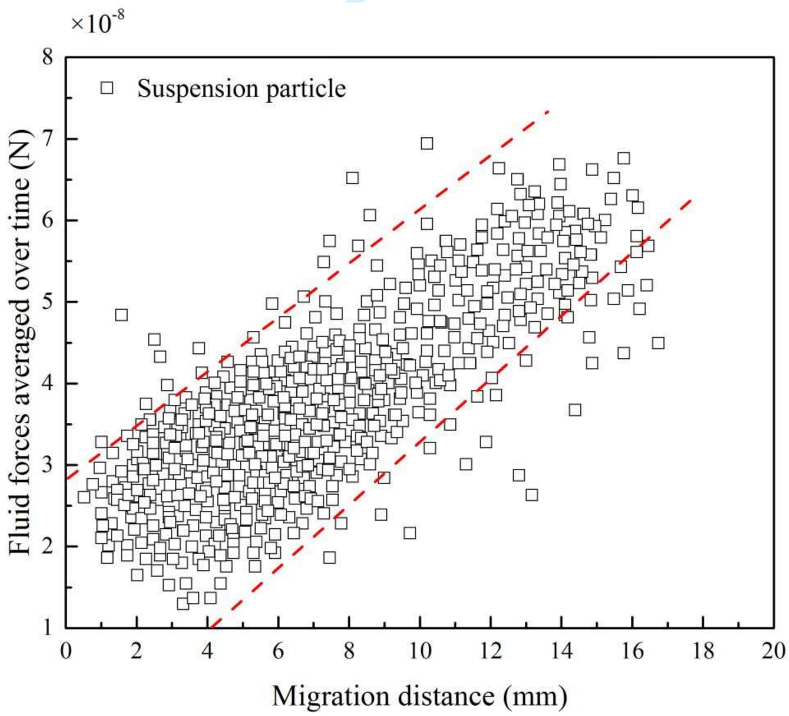

(b)

Figure 17 Relationship between the average particle-fluid interaction force during erosion and migration distance for the suspension particles in the case of F_c=15%, C=70 g/L, and i=0.25 (a) at the end of erosion; (b) during internal erosion